ADVANCED FUNCTIONAL MATERIALS
www.afm-journal.de

High-Density Boron Nitride Nanotube Composites via Surfactant-Stabilized Lyotropic Liquid Crystals for Enhanced Space Radiation Shielding

Young-Kyeong Kim, Ik Jae Lim, Hongjin Lim, Yongbi Joo, Jueun Park, Md Monir Hossain, Hyunjin Cho, Nam-Ho You, Seokhoon Ahn, Hunsu Lee, Sang Seok Lee, Yongho Joo, Se Youn Moon, Hee Il Yoo, Calista Lum, Cheol Park, Siyoung Q. Choi, and Se Gyu Jang**

Despite significant technological advancements in space exploration, human space travel and colonization remain limited by the health risks associated with space radiation. Boron nitride nanotubes (BNNTs) have been proposed as an advanced material for space applications due to their high specific strength and efficient radiation shielding capabilities. However, the practical implementation of BNNTs has been slow, primarily due to technological challenges in fabricating structural materials incorporating BNNTs. In this study, a method is presented for fabricating high-density BNNT films that are mechanically robust, exhibit high thermal conductivity, and effectively attenuate space radiation. The key advancement enabling high-density BNNT films is the successful preparation of BNNT liquid crystals (LCs), achieved through the strategic use of a commercial dodecylbenzenesulfonic acid surfactant. This surfactant ensures exceptional BNNT stability in aqueous dispersion, even at concentrations exceeding the LC phase transition threshold. Simulations, estimating the equivalent radiation dose to the human body in space, indicate that a high-density BNNT film with a surface density of 50 g cm^{-2} reduces the total dose equivalent rate by 56% compared to zero shielding. This enhancement would allow astronauts to extend their mission duration on the lunar surface by a factor of two.

1. Introduction

In recent years, space exploitation has become essential for sustainable human development, extending beyond mere scientific curiosity. Its significance is further underscored by the increasing involvement of private space enterprises.[1,2] However, space radiation—comprising galactic cosmic rays (GCRs) and solar energetic particles (SEPs), which primarily consist of high-energy protons, helium nuclei, heavier ions, and electrons—poses a major challenge to astronaut health.[2–6] These high-linear energy transfer (LET) radiations induce ionization in biological tissues, leading to detrimental effects such as DNA damage, increased cancer risk, genetic mutations, and cell death.[7–11] To mitigate space radiation risks, hydrogen-rich materials, such as high-density polyethylene (HDPE), have been employed as efficient moderators. Their

Y.-K. Kim, I. J. Lim, H. Lim, Y. Joo, J. Park, M. M. Hossain, S. Ahn, S. S. Lee, Y. Joo, S. G. Jang
Functional Composite Materials Research Center
Institute of Advanced Composites Materials
Korea Institute of Science and Technology
Wanju, Jeonbuk 55324, Republic of Korea
E-mail: segyu.jang@kist.re.kr

Y.-K. Kim, I. J. Lim, S. Q. Choi
Department of Chemical and Biomolecular Engineering
Korea Advanced Institute of Science and Technology (KAIST)
Daejeon 34141, Republic of Korea
E-mail: sqchoi@kaist.ac.kr

The ORCID identification number(s) for the author(s) of this article can be found under https://doi.org/10.1002/adfm.202510716

DOI: 10.1002/adfm.202510716

Y.-K. Kim, I. J. Lim, S. Q. Choi
KAIST Institute for the NanoCentury
Korea Advanced Institute of Science and Technology (KAIST)
Daejeon 34141, Republic of Korea

Y. Joo
Department of Chemistry
Gachon University
1342 Seongnam-daero, Sujeong-gu, Seongnam-si, Gyeonggi-do 13120, Republic of Korea

J. Park
Department of JBNU-KIST Convergence
Research Institute of Physics and Chemistry
Jeonbuk National University
Jeonju 54896, Republic of Korea

H. Cho
Department of Materials and Parts of Secondary Battery
Jeonju Kijeon College
Jeonju 54989, Republic of Korea

N.-H. You
Carbon Composite Materials Research Center
Institute of Advanced Composite Materials
Korea Institute of Science and Technology (KIST)
Wanju, Jeonbuk 55324, Republic of Korea

interactions with hydrogen atoms facilitate energy loss through ionization and scattering when exposed to high-energy charged particles.[12–19] In addition to primary space radiation, secondary radiation—including neutrons, gamma rays, and other energetic particles—arises when primary radiation interacts with the exteriors of space vehicles or with lunar and Martian regolith (**Figure 1a**).[20–22] Among the various forms of secondary radiation, backscattered neutrons from the lunar and Martian surfaces—accounting for ≈15–20% of the total radiation dose—pose a particular concern due to their high relative biological effectiveness (RBE) and associated radiation weighting factors.[23–26]

According to the International Commission on Radiological Protection (ICRP) Publication 60 (1990), which provides radiation protection guidelines, the radiation weighting factor for neutrons—used to account for the biological impact of different radiation types—is energy-dependent and typically 5 to 20 times higher than that of photons and electrons (e.g., X-rays and gamma rays).[16,17] Therefore, the moderation of secondary and backscattered neutrons must be carefully addressed to ensure the success of long-term space missions and the development of safe habitats on the Moon and Mars.

Boron nitride nanotubes (BNNTs), having a 2D honeycomb structure via sp^2 hybridization of boron and nitrogen atoms, have garnered significant attention over the past decade due to their unique properties, making them well-suited for space applications. These properties include high specific strength, excellent oxidation resistance, and superior thermal conductivity.[27–30] Additionally, BNNTs' high boron content—constituting 50% of their composition—provides exceptional thermal neutron absorption capabilities, making them highly promising as a space radiation shielding material (Figure 1b).[18,30–36] In neutron capture processes, fast neutrons are first slowed to thermal neutrons by hydrogen-rich materials before being captured through nuclear reactions with the natural isotope of ^{10}B in BNNT.[13,16,37] Therefore, fabrication of stacked layers combining hydrogen-rich polymers and BNNTs has been pursued to synergistically improve the neutron radiation shielding efficiency.[18,30,38–41] However, achieving high-density BNNT films to maximize shielding efficiency remains challenging due to several intrinsic obstacles in BNNT processing. These include their high surface area, the inert nature of BNNT surfaces that hinders surface modification, and the difficulty of preparing stable BNNT dispersions at high concentrations.[41–44] As a result, most BNNT films to date have been limited to fragile lab-scale "bucky papers" with low BNNT densities of ≈0.3–0.43 g cm^{-3}[45–47] produced via vacuum filtration (left optical images in Figure 1c), which is significantly lower than the theoretical density of individual BNNTs (1.38 g cm^{-3}).[48] To enable the early adoption of BNNTs as a next-generation space radiation shielding material, the development of large-scale, high-density, and mass-producible fabrication technologies is urgently needed.

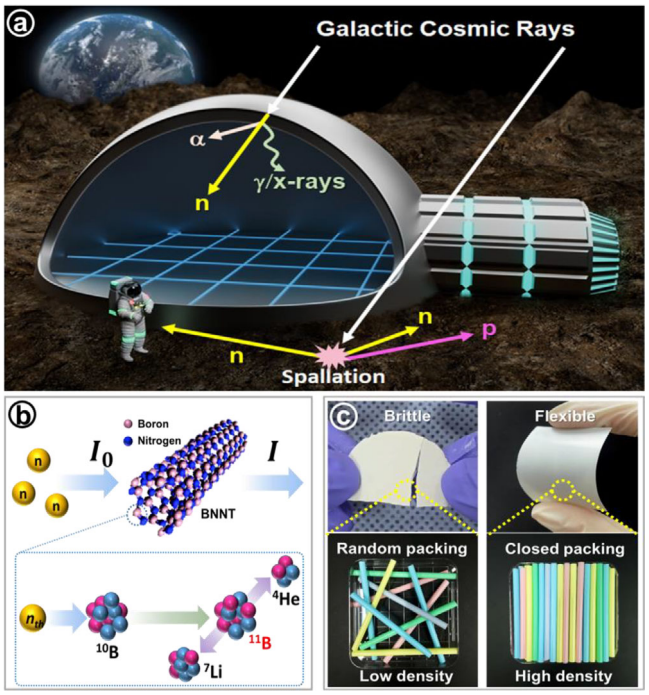

Figure 1. a) Schematic illustration of space radiation on the surfaces of the Moon and Mars. In addition to galactic cosmic rays (GCR) and solar energetic particles (SEP), secondary radiation is generated by interactions with shelter exteriors, vehicles, and regolith. b) Schematic representation of how boron (^{10}B) in boron nitride nanotubes (BNNTs) attenuates thermal neutrons. c) Optical images of BNNT bucky paper (left) and a BNNT film fabricated from a BNNT liquid crystal (right). The high alignment of BNNTs in the film leads to increased lateral packing and BNNT density in the film, illustrated using a straw model.

Recently, lyotropic liquid crystals (LCs) of carbon nanotubes (CNTs) have attracted significant attention due to their unidirectionally aligned nanostructure, which enables a high packing density of CNTs.[49–52] Their exceptional electrical conductivity and mechanical strength—properties rarely achieved by conventional materials—have driven the advancement of CNT-based fibers and films utilizing lyotropic LCs. Similar to CNTs, BNNT LCs have also been successfully developed using surface protonation with a superacid, such as chlorosulfonic acid (CSA).[38,53] Despite this progress, an eco-friendly solvent such as water would be preferable for large-scale production, as the use of harsh superacids poses environmental and health risks. As a more sustainable approach for industrial BNNT applications, we recently

H. Lee
Ramp Convergence Research Center
Institute of Advanced Composites Materials
Korea Institute of Science and Technology
Wanju, Jeonbuk 55324, Republic of Korea
S. Y. Moon, H. I. Yoo
High-enthalpy Plasma Research Center
Jeonbuk National University
546 Bongdong-ro, Bongdong-eup, Wanju-gun, Jeollabuk-do 55317, Republic of Korea
C. Lum
Department of Physics
University of California
Irvine, CA 92697, USA
C. Park
Advanced Materials Processing Branch
NASA Langley Research Center
Hampton, VA 23681, USA

introduced a method for preparing aqueous BNNT liquid crystals (LCs) and BNNT/polymer composite fibers using a specifically designed copolymer dispersant, poly(vinylpyrrolidone-*r*-hydroxyethyl vinylimidazolium bromide) (P(VP-r-QVI)).[54] However, for future industrial deployment of BNNT LCs, the development of a cost-effective, commercially available stabilizer capable of maintaining dispersion stability at extremely high concentrations remains a priority.

Various commercial surfactants, including cetyltrimethylammonium bromide (CTAB), sodium dodecyl sulfate (SDS), dodecyltrimethylammonium bromide (DTAB), and Pluronic F108, have been reported to successfully disperse BNNTs in aqueous media.[55] However, achieving highly concentrated BNNT dispersions using surfactants remains a significant challenge. This difficulty arises because, beyond a certain concentration, excess surfactant that cannot adsorb onto the nanoparticle surface instead self-assembles into micelles or other aggregated structures during dispersion concentration. If these micelles are significantly smaller than the nanoparticles, they can induce flocculation through the depletion mechanism.[56] Thus, when using surfactants to disperse nanoparticles in aqueous media, the ratio of surfactant to nanoparticles is critical. While still debated, it is generally understood that surfactants can self-assemble on nanotube surfaces in various configurations, including random adsorption, hemi-micelles, or cylindrical micelles.[57] The interfacial adsorption behavior and formation of aggregated structures depend on several factors, including surfactant type and concentration, hydrophobic/hydrophilic interactions, binding affinity between the head group and nanotube surface, and solvent properties. For instance, SDS molecules have been observed to aggregate as rolled-up half-cylinders on multi-walled CNT surfaces,[58,59] while cylindrical micelles of SDS wrapping single-walled CNTs have also been reported.[60] Interestingly, SDS can self-assemble into bilayers when adsorbed onto rough glass surfaces (RGS) in aqueous solutions.[61] This occurs because SDS head group adsorption onto RGS reduces hydration volume and electrostatic repulsion, thereby decreasing the head group area at the solid-liquid interface. Additionally, SDS's single alkyl chain structure facilitates interdigitation of tail groups, stabilizing bilayers or vesicles in aqueous media.[62] Inspired by these findings, we propose that highly concentrated BNNT dispersions can be achieved through the strategic selection of surfactants that self-assemble into bilayer or vesicle structures. This approach would optimize interactions between the surfactant head groups and the BNNT surface while promoting strong interdigitation, thereby minimizing surfactant dissociation into the dispersion medium and reducing micelle formation during dispersion concentration for the preparation of BNNT LCs.

Here, we report the use of a commercial dispersant, dodecylbenzenesulfonic acid (DBSA), which self-assembles into a bilayer structure on the BNNT surface, enabling sufficient dispersion stability to form lyotropic liquid crystals (LCs). The bilayer formation of DBSA was systematically characterized through thermogravimetric analysis (TGA) to determine adsorbed DBSA areal density, along with surface tension measurements of BNNT dispersions. Unlike neutralized commercial surfactants such as SDS, which induce BNNT flocculation at high concentrations, DBSA-stabilized BNNTs (DBSA-BNNTs) exhibited excellent dispersion stability and successful LC phase transition. This was confirmed using Turbiscan analysis, optical microscopy (OM), and polarized optical microscopy (POM). By leveraging DBSA-BNNT LCs, we successfully fabricated high-density BNNT films (≈1.3 g cm^{-3}, more than three times higher than conventional bucky paper) through shear force application via doctor blade coating. Systematic characterizations using scanning electron microscopy (SEM), image analysis, and POM revealed that BNNTs within the LC film were highly oriented parallel to the coating direction, resulting in a high lateral packing density of nanotubes. Compared to lab-scale BNNT bucky paper, the DBSA-BNNT films exhibited significantly enhanced physical properties, including improved flexibility (right optical images in Figure 1c), superior thermal conductivity (≈3.1 W m^{-1}·K, twice that of bucky paper), and a high thermal neutron linear attenuation coefficient (≈2.2 mm^{-1}, 3.7 times higher than bucky paper). Finally, the superior radiation shielding effectiveness of DBSA-BNNT films over conventional aluminum was demonstrated through simulations using the On-Line Tool for Assessment of Radiation in Space (OLTARIS) simulation.

2. Results and Discussion

In aqueous nanoparticle dispersions, the surfactant-to-nanoparticle ratio is critical to prevent micelle formation, which can lead to depletion flocculation.[56] To mitigate this effect, excess free surfactants (SDS and DBSA) in deionized (DI) water were removed through a centrifugation and decantation process. Specifically, the surfactant-dispersed BNNTs were centrifuged, allowing the BNNTs to sediment at the bottom of a conical tube. The supernatant, containing the excess free surfactants, was carefully decanted. The resulting BNNT sediment was then redispersed in fresh DI water. **Figure** 2a,b presents Turbiscan data illustrating the long-term dispersion stability of BNNTs in aqueous media. Briefly, Turbiscan measures transmittance intensity—proportional to BNNT concentration—according to the Beer-Lambert law, recording transmittance changes (ΔT) over time. A gradual increase in ΔT (≈17.5% after 24 h) for the SDS-assisted BNNT (SDS-BNNT) dispersion (≈0.3 wt.% BNNT) in Figure 2a indicates partial aggregation and sedimentation. This instability may result from the desorption of SDS molecules from the BNNT surface into the aqueous phase. In contrast, the DBSA-assisted BNNT (DBSA-BNNT) dispersion (≈0.3 wt.% BNNT) exhibited significantly better stability, with ΔT of ≈3.2% after 24 h (Figure 2b). The disparity in stability between SDS-BNNT and DBSA-BNNT dispersions became even more pronounced when the dispersions were concentrated. (Figure 2c (4 wt.% SDS-BNNT, refers to BNNT content only, excluding surfactant) and Figure 2d (12 wt.% DBSA-BNNT, refers to BNNT content only, excluding surfactant)). Optical (OM) and polarized optical microscopy (POM) images of the SDS-BNNT concentrate reveal partial aggregation and flocculation (Figure 2c). However, upon dilution with water, the aggregates were redispersed, demonstrating the reversible stability characteristic of depletion-induced flocculation (Figure S2, Supporting Information).[56] In clear contrast, no aggregation was observed in DBSA-BNNT dispersions even at concentrations up to 12 wt.% (Figure 2d). The presence of clear birefringent textures in the POM image, obtained using crossed polarizers, confirms the formation of a lyotropic liquid crystal (LC) phase—a hallmark of high

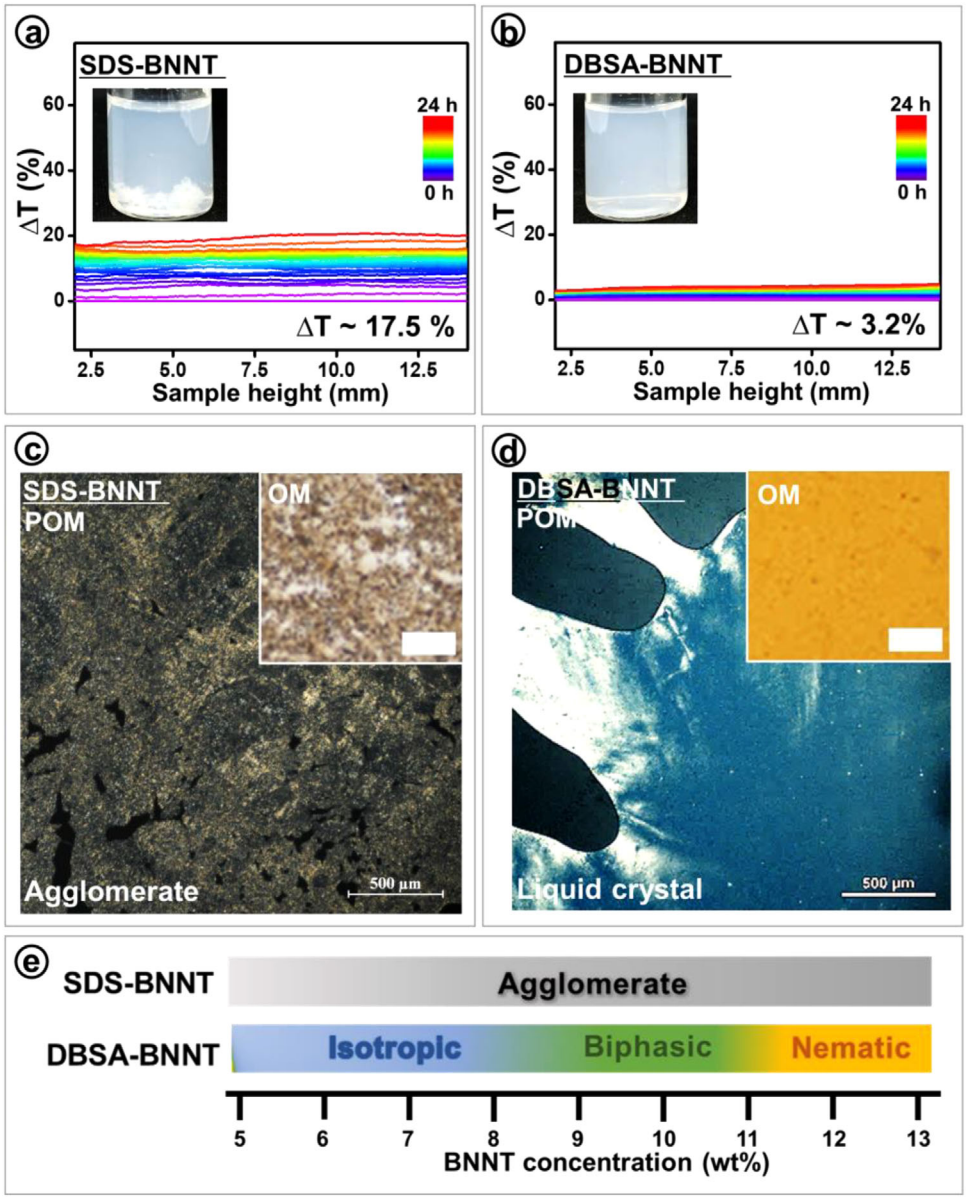

Figure 2. Long-term dispersion stability test results of a) SDS-assisted BNNT (SDS-BNNT) and b) DBSA-assisted BNNT (DBSA-BNNT) aqueous dispersions using Turbiscan. Insets are optical images of the dispersions. Optical (insets) and polarized optical microscope images of c) flocculated SDS-BNNT (≈4 wt.%) and d) DBSA-BNNT (≈12 wt.%) liquid crystal. Scale bars in the insets represent 100 μm. e) Phase diagram illustrating the phase transition from isotropic to biphasic and nematic liquid crystal according to BNNT concentration.

dispersion stability and microscopic lateral order of DBSA-BNNTs (Additional POM images and rheological analysis results, illustrating phase transitions with increasing BNNT concentration, are provided in Figure S1, Supporting Information).[54,63] The phase diagram in Figure 2e shows a transition from an isotropic to biphasic region at the mass concentration of BNNT (C_{BNNT}) ≈ 9 wt.% and to a fully nematic phase at C_{BNNT} ≈ 11 wt.%. The superior dispersion stability of DBSA-BNNTs at high concentrations indicates strong adsorption of DBSA on BNNT surfaces, preventing desorption and subsequent micelle formation, which would otherwise cause depletion flocculation. Based on systematic thermogravimetric analysis and surface tension measurements, we conclude that DBSA molecules self-assemble into a bilayer structure on BNNTs. This self-assembly is driven primarily by the strong interaction between the sulfonic acid head group and the BNNT surface, as well as interdigitation of the aliphatic chains. These findings will be elaborated in the Discussion section (Figure 5).

In the nematic DBSA-BNNT liquid crystal (LC) phase, BNNTs exhibit microscopic ordering with randomly oriented polycrystalline domains. Doctor blade coating, as schematically illustrated in **Figure 3a**, provides key advantages, including large-area uniformity, low material consumption, and rapid processing. During coating, the application of unidirectional shear stress

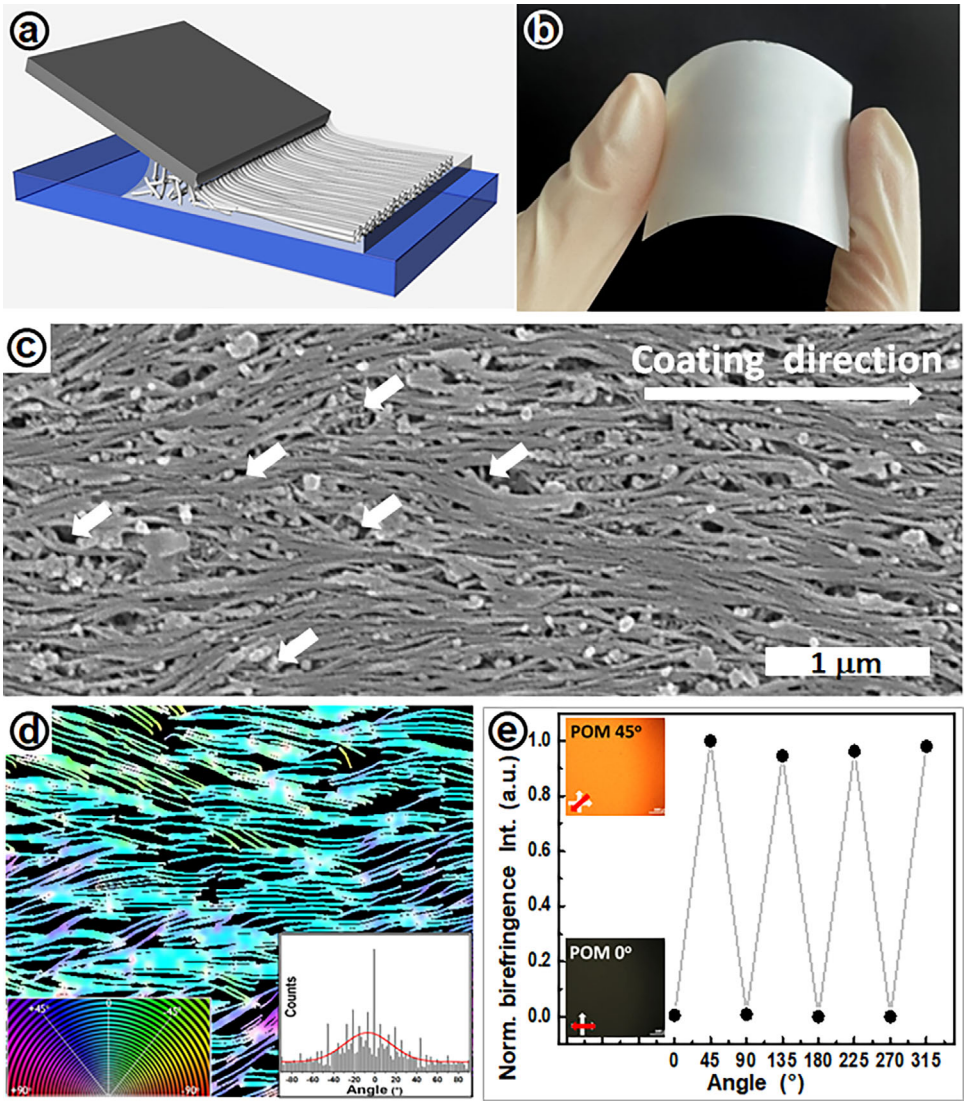

Figure 3. a) Schematic illustration of the coating process using doctor blade, where shear alignment is used to align liquid crystalline DBSA-BNNT dope. b) Optical image showing the flexibility and uniformity of a high-density DBSA-BNNT film. c) SEM top-view image of the DBSA-BNNT film, with white short arrows indicating defect positions caused by impurities such as hBNs and cages. d) Vector angle distribution analysis of the SEM top-view image using ImageJ, demonstrating the high alignment of BNNTs along the shear stress direction. e) Graph and POM images (insets) showing normalized birefringence intensity changes as a function of the film's rotation angle, indicating good BNNT alignment along the coating direction.

(≈1250 s^{-1} shear rate) realigns the polycrystalline BNNT microdomains, forming a film in which BNNT bundles are predominantly aligned along the shear direction. A uniform, flexible, and mechanically robust DBSA-BNNT film was successfully coated onto a polyethylene terephthalate (PET) substrate using a 16 wt.% DBSA-BNNT LC dope, as shown in Figure 3b. The film's thickness can be precisely controlled by adjusting the doctor blade gap size (films with a thickness of 20 µm were used in this experiment as shown in Figure S3, Supporting Information). The top-view SEM image (Figure 3c) reveals BNNT bundles aligned along the coating direction. White arrows indicate representative defect sites caused by BNNT impurities such as shell-like cages and hexagonal boron nitride (hBN) particles.[64] These impurities disrupt the alignment of BNNT bundles, suggesting that the alignment and packing density could be further enhanced by the use of higher-purity BNNTs. To quantitatively analyze alignment, SEM images of DBSA-BNNT bundles were overlaid onto a transparent PET film and processed using ImageJ software. As shown in Figure 3d, vector analysis was performed to assess the orientation angle of BNNTs relative to the coating direction. The corresponding angle distribution analysis (inset in Figure 3d) further confirms a high degree of BNNT alignment along the shear stress direction. POM images in the inset of Figure 3e verify that the DBSA-BNNT film was uniformly coated and free of cracks. Notably, the distinct changes in birefringence intensity observed in POM analysis, depending on the film's rotation angle (Figure 3e), provide clear evidence that BNNTs are highly aligned along the coating direction.

Table 1. Comparison of physical properties between DBSA-BNNT LC Film and bucky paper.

Property	Bucky paper	DBSA-BNNT LC film
Density [g/cm^3]	0.4	1.25
Volume fraction of BNNTs [%]	20	80
Linear attenuation coefficient [mm^{-1}]	0.6	2.2
Thermal conductivity [W/m·K]	1.5	3.13
Mass attenuation coefficient [cm^2/g]	15	17.6

To quantify the degree of alignment, the order parameter (S) of the DBSA-BNNTs in the film was determined by calculating the linear dichroic ratio (D) from the birefringence intensity profile in Figure 3e.[65] The measured intensity ratio $D = I_{max}/I_{min}$ represents the combined effect of birefringence and dichroism. Following Fraser-Beer theory, this was corrected using the geometric factor g to obtain the true linear dichroic ratio $D^* = g \times D_{measured}$. Given the small effective refractive index of DBSA-BNNT ($\Delta n_{eff} = 0.040$[66] from Maxwell-Garnett calculation[67]), the geometric correction factor g is approximated as 1. In addition, the DBSA-BNNT film on glass, which exhibits a gray interference color shown in the Michel-Lévy birefringence chart in Figure S4 (Supporting Information), reflects a small anisotropy in the refractive index of BNNTs, indicating the geometric correction factor can be simplified as 1.[65,68]

The linear dichroic ratio (D) is defined as:

$$\mathbf{D} = \frac{I_{max}}{I_{min}} = \frac{Intensity\ at\ 45°}{Intensity\ at\ 0°\ (or\ 90°)} \quad (1)$$

The order parameter (S) was determined using the simplified Equation (2):[65,68]

$$\mathbf{S} = \frac{\mathbf{D} - 1}{\mathbf{D} + 2} \quad (2)$$

From this calculation, the S value of 0.52 indicates a relatively high degree of nanotube alignment, though not perfectly unidirectional (S = 1). As previously mentioned, the alignment and packing density of BNNTs can be further enhanced by utilizing higher-purity BNNTs, which will be explored in future work.

To demonstrate the advancements of the DBSA-BNNT LC film, we measured key physical properties, including thermal neutron attenuation coefficients, thermal conductivity, density, and volume fraction, as summarized in **Table 1**.

Compared to BNNT bucky paper (≈0.40 g cm^{-3}) fabricated via vacuum filtration of a BNNT dispersion in ethanol, the DBSA-BNNT LC film exhibited a density more than three times higher (≈1.25 g cm^{-3}) due to the high packing of unidirectionally aligned BNNT bundles. This increased density enhances both the film's structural robustness and its neutron shielding effectiveness, represented by the linear attenuation coefficient (μ), as described by Beer-Lambert's law:

$$I = I_0 e^{-\mu t} \quad (3)$$

where I_0 is the incident radiation intensity, I is the transmitted intensity, and t is the sample thickness. The measured linear attenuation coefficient of the DBSA-BNNT LC film using an Americium-Beryllium (Am/Be) neutron source was 2.2 mm^{-1}, ≈3.7 times higher than that of BNNT bucky paper (≈0.6 mm^{-1}). This improvement is primarily due to the higher density of boron atoms in the DBSA-BNNT LC film at the same thickness.[69,70] Additionally, the mass attenuation coefficients, which describe the fraction of thermal neutrons attenuated per unit mass of material, were measured as ≈15 cm^2 g^{-1} for BNNT bucky paper and ≈17.6 cm^2 g^{-1} for DBSA-BNNT LC film. These values are significantly higher than those of conventional aerospace shielding materials, including aluminum (≈0.03 cm^2 g^{-1}),[71] polyethylene (≈0.34 cm^2 g^{-1}),[72] epoxy with 5 wt.% boron carbide (≈0.28 cm^2 g^{-1}),[73] and aluminum with 30 wt.% boron carbide (≈7.46 cm^2 g^{-1}).[74] This highlights the superior efficiency of BNNT-based materials for thermal neutron shielding with minimal mass, a critical factor for optimizing fuel efficiency and reducing flight costs. The advanced properties of the high-density DBSA-BNNT film over BNNT bucky paper are visually represented in the radar chart in **Figure 4b**. Aside from the mass attenuation coefficient, all other properties—density, volume fraction, linear attenuation coefficient, and thermal conductivity—were at least twice as high. These superior characteristics primarily result from the higher BNNT packing density in the film, which increases nanotube contact points, thereby enhancing mechanical robustness and improving thermal conduction pathways. Notably, further improvements in these properties can be achieved by using higher-purity BNNTs, which would reduce defect points and voids within the film.

The On-Line Tool for Assessment of Radiation in Space (OLTARIS), developed by NASA, is an integrated simulation tool used to assess the effects of space radiation on various objects, including humans.[75] Using OLTARIS, we evaluated the total dose equivalent rate (TDER) through high-density DBSA-BNNT film and aluminum (Al) shields under space radiation on the lunar surface over a one-day period, as shown in Figure 4c,d (detailed simulation conditions are provided in the experimental section). Note that mass thickness, defined as the mass of shielding material per unit surface area, is a parameter for optimizing space radiation protection while minimizing weight. The TDER values, representing the total biological damage caused by radiation exposure—including GCR and albedo effects initially decrease rapidly with increasing mass thickness up to 50 g cm^{-2}. Then, TDER values rise as a shoulder until mass thickness reaches 150 g cm^{-2}. Compared to the TDER values for an Al shield, those for the DBSA-BNNT film are approximately 15% lower across the mass thickness range of 10 to 250 g cm^{-2}, demonstrating the superior shielding efficiency of BNNT-based materials. The experimentally measured dose equivalent rate from charged particles on the lunar surface, reported by Chang'E 4, is ≈1.37 mSv per day,[76] closely matching the OLTARIS simulation result of ≈1.35 mSv per day for an Al shield with a mass thickness of 0.001 g cm^{-2}. The DBSA-BNNT shield at 50 g cm^{-2} mass thickness reduces the TDER to ≈0.6 mSv per day (≈44% of the unshielded TDER), a value comparable to the experimentally measured dose equivalent rate aboard the International Space Station (ISS) (≈0.52 mSv per day), proven dose equivalent rate value to be proper for astronauts to stay for long-term mission.[76] Furthermore, this suggests that a DBSA-BNNT shield at 50 g cm^{-2}

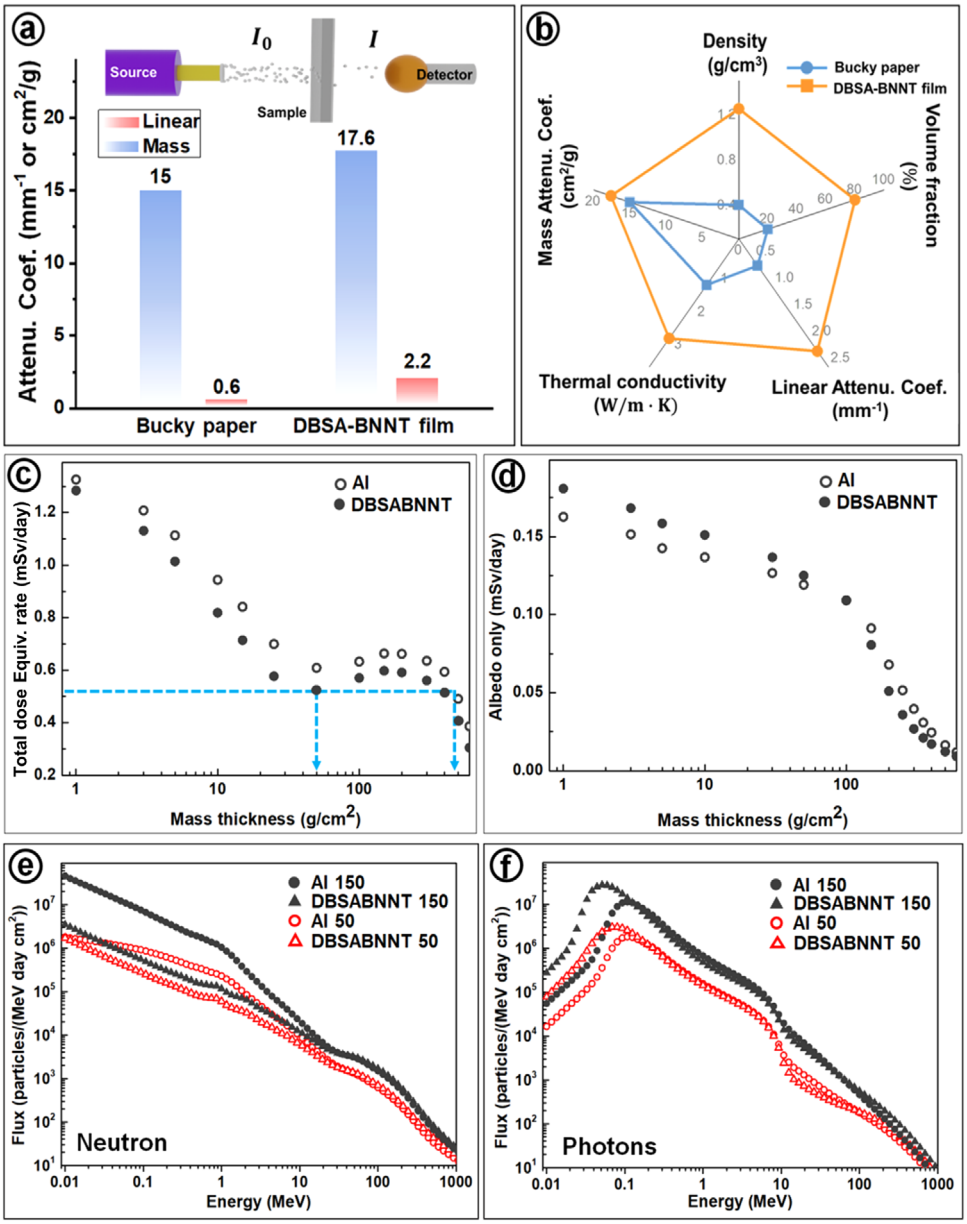

Figure 4. a) Linear and mass attenuation coefficients of BNNT bucky paper and high-density DBSA-BNNT film, demonstrating their thermal neutron shielding effectiveness. The inset schematic illustrates the attenuation coefficient measurement process based on Beer-Lambert's law. b) Radar chart comparing the superior physical properties of the DBSA-BNNT film—such as density, volume fraction, linear/mass attenuation coefficients, and thermal conductivity—against those of bucky paper. c) Total dose equivalent rate and d) dose equivalent rate from albedo radiation on the lunar surface as a function of mass thickness for aluminum (Al, open circles) and DBSA-BNNT shields (filled circles), simulated using OLTARIS. e) Neutron and f) photon fluxes reaching the target after passing through Al and DBSA-BNNT shields of varying mass thicknesses of 50 g cm^{-2} (open circles for Al and open triangles for DBSA-BNNT) and 150 g cm^{-2} (filled circles for Al and filled triangles for DBSA-BNNT).

could allow astronauts to stay on the lunar surface for twice as long as without it.

The GCR shielding effectiveness ((dose equivalent rate at zero-shield condition)/(dose equivalent rate at corresponding mass thickness)) of the DBSA-BNNT shield is even more pronounced when compared to aluminum. The TDER value of a 50 g cm^{-2} DBSA-BNNT shield corresponds to that of an Al shield with a much higher mass thickness of ≈400 g cm^{-2} (as indicated by the blue dashed lines in Figure 4c). Given that the dose equivalent rate values from albedo radiation in Figure 4d are similar for both Al and DBSA-BNNT shields and relatively small compared to the overall TDER, the increase in TDER values observed between 50 and 150 g cm^{-2} (shoulder) is likely due to secondary radiation effects. These include backscattered neutrons, protons, muons, and pions generated from GCR interactions with shielding materials. The BNNT films, owing to the presence of ^{10}B isotopes, can effectively moderate these backscattered neutrons. OLTARIS flux-versus-energy analysis in Figure 4e supports this, showing

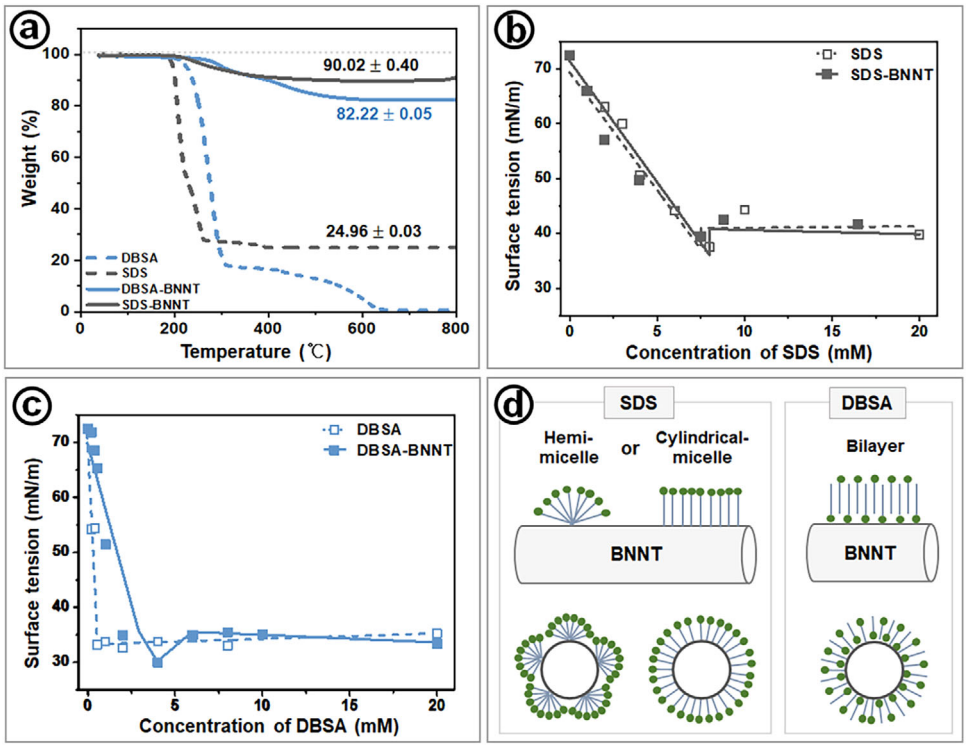

Figure 5. a) TGA analysis results of DBSA, SDS, DBSA-BNNT, and SDS-BNNT, used to estimate the amounts of adsorbed surfactants. Surface tension measurements of b) SDS and SDS-BNNT and c) DBSA and DBSA-BNNT dispersions at the air-water interface, plotted as a function of surfactant concentration at room temperature. d) Schematic illustration depicting the aggregated structures of SDS and DBSA on the BNNT surface.

that neutron flux to the target (at 10 keV energy) was significantly reduced from ≈4.7×10^7 to ≈3.5×10^6 neutrons/(MeV·cm^2·day) when replacing 150 g cm^{-2} of Al with an equivalent mass thickness of DBSA-BNNT shield. Additionally, neutron flux through the DBSA-BNNT shield remained significantly lower up to an energy level of ≈30 MeV for both 50 and 150 g cm^{-2} mass thicknesses. Although the DBSA-BNNT shield exhibited slightly higher photon flux compared to Al, this increase has a negligible effect on the TDER value, given that the neutron weighting factor is 5 to 20 times higher than that of photons. These results strongly indicate that DBSA-BNNT shield not only provide effective shielding against GCR but also significantly reduce harmful backscattered neutron radiation, a key limitation of conventional aluminum shielding materials.

3. Discussion

As demonstrated in the experimental results for concentrated SDS-BNNT dispersion, partial aggregation was observed as the SDS-BNNT concentration increased. Since most free surfactants were removed from the dispersion via centrifugation and decantation processes, it is presumed that flocculation-inducing micelles are primarily generated due to the desorption of SDS from the BNNT surface into the aqueous phase. Interestingly, no flocculation was observed in the DBSA-BNNT dispersion, even at high concentrations. This may be attributed to the stronger and more stable adsorption of DBSA onto the BNNT surface compared to SDS, making it less prone to desorption during the concentration process. Direct observation of the self-assembled structure of DBSA on BNNT is technically challenging due to low transmission electron microscope (TEM) contrast. It should be noted that the following discussion is based on indirect evidences, as direct observation of the adsorbed surfactant structures such as cryo-TEM was technically challenging. More detailed explanations regarding the estimation of surface areal density of surfactants on BNNTs, as well as the energy-dispersive X-ray spectroscopy (EDX) data, are provided in Supporting Information S1. We will leave our hypothesis regarding bilayer formation as an open question for the readers. To indirectly investigate DBSA adsorption, we characterized its surface areal density using the method proposed by Grossiord et al.[77] **Figure 5a** presents the TGA analysis of DBSA, SDS, DBSA-BNNT, and SDS-BNNT, which was used to estimate the amounts of adsorbed surfactants. Given BNNT's high thermal stability with negligible mass loss up to 800 °C, the observed TGA mass reductions were solely attributed to the combustion of bound SDS and DBSA. Taking into account residual sodium content after TGA experiment, the amount of SDS adsorbed per gram of BNNT was approximately 76 mg g^{-1} (≈0.26 mmol g^{-1}). In contrast, since DBSA leaves no residue upon combustion, its adsorption was determined to be 217 mg g^{-1} (≈0.66 mmol g^{-1}), ≈2.5 times higher than SDS. Considering the BNNTs used in this study have an average diameter of ≈4.5 nm and ≈2.5 walls,[78] their estimated surface area is ≈760 m^2 g^{-1} (for comparison, multi-walled CNTs and single-walled CNTs typically exhibit surface areas of 100–150 m^2 g^{-1} and over 1000 m^2 g^{-1}, respectively). Based on this, the areal density of SDS and DBSA on the BNNT surface was calculated as ≈2.07 and ≈5.26 molecules/nm^2, respectively. Previous studies have

reported SDS adsorption densities on CNT surfaces in the range of 2.2–2.7 molecules/nm^2, with surfactants primarily forming hemispherical micelles oriented with their hydrophilic heads facing the aqueous phase.[77,79–81] In the case of SDS, adsorption occurs primarily via relatively weak van der Waals interactions, allowing a substantial fraction to be released into the aqueous phase in dynamic equilibrium. This desorption during concentration leads to depletion-induced flocculation, as observed in our experimental results.

Figure 5b,c presents the surface tension measurements of SDS, SDS-BNNT, DBSA, and DBSA-BNNT dispersions at the air-water interface, plotted as a function of surfactant concentration at room temperature. When only SDS or DBSA surfactants are present (open squares with dashed lines), the surface tension at the air-water interface decreases continuously with increasing surfactant concentration until it reaches the critical micelle concentration (CMC). Above the CMC, excess surfactants self-assemble into aggregated structures such as micelles, leading to a plateau in surface tension despite further increases in surfactant concentration. For surface tension measurements of SDS-BNNT and DBSA-BNNT dispersions according to the addition of surfactants, the BNNTs were dispersed with a minimum amount of each surfactant to get relatively stable dispersions. Then, the BNNT sediments, after centrifugation to remove unbound surfactants, were diluted to prepare dispersions with 0.2 mM DBSA and 1 mM SDS based on the measured adsorbed amount of surfactants on BNNTs by TGA. Then, additional surfactants were added to find critical micelle concentration values. In Figure 5b, the change in surface tension of SDS-BNNT dispersion follows a trend nearly identical to that of the SDS-only dispersion, with both CMC_{SDS} and $CMC_{SDS\text{-}BNNT}$ values ≈ 8 mM. In contrast, as shown in Figure 5c, the dispersion containing only DBSA exhibits a rapid decrease in surface tension, reaching a CMC_{DBSA} of ≈0.53 mM.[62] However, the $CMC_{DBSA\text{-}BNNT}$ for the DBSA-BNNT dispersion is much higher, ≈ 4 mM. This higher $CMC_{DBSA\text{-}BNNT}$ indicates that DBSA exhibits stronger thermodynamic affinity for the BNNT surface compared to the air-water interface, resulting in preferential equilibrium adsorption to the BNNT surface. Despite SDS and DBSA having similar hydrophobic tails, this rapid adsorption of DBSA cannot be fully explained by hydrophobic/hydrophilic interactions or van der Waals attraction alone. A more plausible explanation is that the head group of DBSA interacts specifically with the BNNT surface, enabling higher areal density adsorption. For stable DBSA-BNNT dispersion in aqueous solutions, DBSA molecules must self-assemble into a bilayer structure with head groups on outer layer facing the aqueous phase, facilitated by the interdigitation of hydrophobic tails, as shown in Figure 5d.

The aggregated structure of surfactants in aqueous solution can be predicted using the molecular packing parameter (P),[82] which is defined as $P = v/(a_0 l)$, where v is the tail volume of the surfactant molecule, l is the tail length, and a_0 is the area occupied at the aggregated surface. Generally, when $P \leq 1/3$, spherical micelles are favored; when $1/3 \leq P \leq 1/2$, cylindrical micelles are preferred; and when $1/2 \leq P \leq 1$, vesicles or bilayers are the predominant self-assembled structures. For example, literature values for a_0, l, and v of SDS are reported as 0.53 – 0.63 nm^2 (at the air-liquid interface), 1.67 nm, and 0.35 nm^3, respectively.[83,84] Therefore, the calculated P value ranges from ≈0.33 to 0.39, indicating that SDS primarily forms spherical or cylindrical micelles in aqueous solution, which aligns well with existing literature.[58,59,85] Similarly, SDS likely adsorbs onto hydrophobic surfaces such as CNTs or BNNTs in a hemispherical or cylindrical micellar form if adsorption is driven solely by hydrophobic/hydrophilic interactions. Interestingly, SDS can also self-assemble into bilayers when adsorbed onto a rough glass surface (RGS) in aqueous solution.[61] This phenomenon occurs because SDS head groups adsorb onto the RGS, reducing hydration volume and electrostatic repulsion, which significantly decreases the a_0 value at the solid-liquid interface. Additionally, the single alkyl chain structure of SDS allows interdigitation of tail groups, stabilizing bilayer or vesicular formations in aqueous solution.[62] Similarly, at high concentrations, DBSA self-assembles into bilayers, where the sulfonic acid head groups are hydrogen bonded by acid-soap dimer formation. This dimer formation reduces electrostatic repulsion between head groups, decreases the a_0 value, and also increases the effective tail volume, promoting self-assembly into vesicle. Based on TGA results from Figure 5a, the areal density of DBSA on the BNNT surface was calculated to be ≈5.26 molecules/nm^2, which is about 2.5 times higher than that of SDS. Given the van der Waals radius of the sulfonate head group, such a high areal density—exceeding 4 molecules/nm^2 for DBSA[77,86] seems unrealistic unless a bilayer structure is assumed. If DBSA (or DBSA dimers) adopts a bilayer configuration on BNNT, the calculated areal density of adsorbed DBSA is approximately 2.63 molecules nm^{-2}. Using the estimated a_0 value of 0.38 nm^2 molecule^{-1} (≈ 1/areal density) and l and v values of ≈1.67 nm and 0.35 nm^3, the calculated P value is around 0.59, indicating vesicle formation.

The formation of such a bilayer structure requires strong adsorption of the DBSA head groups onto BNNT. Several studies support the existence of favorable interactions between sulfonic acid groups and boron nitride surfaces. Hydrogen bonding or dative bonding between the electron lone pairs of oxygen in the sulfonic acid group and the partially positively charged boron atoms of hexagonal boron nitride (hBN) has been reported.[87] Methanesulfonic acid adsorption onto hBN via protonation has also been documented.[88] Additionally, Ginestra et al. reported that chlorosulfonic acid can protonate nitrogen atoms on the BNNT surface, inducing a positive surface charge.[53] Furthermore, Lisjak et al. demonstrated that the sulfonic acid head group of DBSA covalently bonds to the surface of barium ferrite nanoplatelets via oxygen bridging, while van der Waals forces between DBSA tails facilitate an interdigitated bilayer structure.[89] Similar to these findings, DBSA's sulfonic acid head group likely interacts favorably with the BNNT surface, enhancing adsorption. In addition, DBSA's acid-soap dimer formation, π-π stacking of benzene rings, and interdigitation of a second layer with head groups facing the aqueous phase further increase the areal density of DBSA on BNNT. This strong adsorption prevents DBSA desorption into the aqueous phase, thereby limiting free micelle formation and depletion-induced flocculation at high concentrations.[62] These findings, supported by literature and rough estimations, strongly suggest that the DBSA head group adsorbs onto the BNNT surface, leading to bilayer formation rather than hemispherical or cylindrical micelles. This insight provides an efficient approach for preparing highly concentrated dispersions and lyotropic liquid crystals (LCs) with BNNTs in an eco-friendly aqueous media,

facilitating the fabrication of advanced composites such as fibers and films with high BNNT density.

4. Conclusion

A high-density BNNT film, with a density more than three times that of conventional bucky paper, was successfully fabricated through the high lateral packing of BNNTs induced by the shear alignment of lyotropic BNNT liquid crystals (LCs). The judicious selection of a commercial DBSA surfactant, which self-assembles into a bilayer structure on the BNNT surface, provides exceptional stability for BNNTs in aqueous dispersion, even beyond the LC phase transition concentration. The bilayer configuration of DBSA on the BNNT surface was confirmed through both theoretical analysis and systematic characterizations, including TGA and surface tension measurements. The high-density BNNT films, featuring laterally aligned BNNTs, exhibit superior physical properties compared to lab-scale bucky paper. These include enhanced mechanical robustness with flexibility, a thermal conductivity approximately twice as high, and a linear adsorption coefficient for thermal neutrons that is about 3.7 times greater. Using OLTARIS simulations to model space radiation effects on the lunar surface, it was found that the total dose equivalent rate through the high-density BNNT film reduces space radiation exposure by ≈15% more than conventional aluminum exteriors. Furthermore, a DBSA-BNNT film with a mass of 50 g cm^{-2} reduces the total dose equivalent rate by 56% compared to zero shielding—achieving radiation protection levels similar to those on the ISS. This shielding efficiency would allow astronauts to extend their mission duration on the lunar surface by a factor of two. These findings inspire materials scientists to develop high-BNNT-content composites with exceptional robustness and radiation shielding efficiency—critical advancements for future lunar and Martian exploration.

5. Experimental Section

Purification of BNNTs: Boron nitride nanotubes (BNNTs), synthesized with high-temperature 60 kW RF inductively coupled plasma (RF-ICP), were provided by the High-enthalpy Plasma Research Center at Jeonbuk National University. The as-synthesized BNNTs, containing hexagonal boron nitride (h-BN), various BN derivatives, and boron-based impurities, were purified according to the reported purification method.[90] Briefly, BNNTs were calcined at 650 °C for 6 h in the air to oxidize amorphous boron. Then, they were mechanically stirred in DI water (1 g BNNT in 1L water) using a High Shear Mixer (L5M-A, Silverson) at 5,000 rpm for 20 min. The BNNT aggregates were subsequently filtered using a 300-mesh (35 µm) metal filter. The agitation-filtration cycle was repeated 15 times until the filtrate appeared visually clear. The purified BNNTs were dispersed in a binary solvent mixture (1 wt.%) consisting of tert-butyl alcohol (purchased from Sigma-Aldrich, ≥99.5%) and DI water (40:60 w/w). Then, the dispersion was freeze-dried for 2 days.

Preparation of DBSA-BNNT Dispersion and Lyotropic BNNT Liquid Crystal: 4-Dodecylbenzenesulfonic acid (DBSA, soft type, mixture, purchased from TCI, ≥95.0%) was added with BNNTs into DI water (3 mg DBSA and 3 mg BNNT in 1 mL water). The mixture was then subjected to bath sonication for 60 min. Then, the DBSA-BNNT dispersion was centrifuged at 9,500 rpm for 40 min to remove excess DBSA surfactants. It is important to note that centrifugation separates phases but does not alter the chemical potential or bulk concentration of the DBSA surfactant. Therefore, only the free DBSA molecules present in the initial BNNT dispersion medium were removed by centrifugation and subsequent decantation. To estimate the relative amount of DBSA remaining after this process, the pH values of the initial BNNT dispersion (pH ≈ 2.4) was measured, the supernatant containing free DBSA (pH ≈ 2.5), and the redispersed BNNTs stabilized with DBSA in fresh deionized (DI) water (pH ≈ 3.5). A rough estimation using the acid dissociation constant (Ka) equation suggests that the residual DBSA—comprising both DBSA bound to the surface of BNNTs and free DBSA in the dispersion medium—was approximately 20% of the amount initially added to the BNNT dispersion. (Supporting Information S2) After centrifugation, the supernatant containing unbound DBSA was carefully decanted and discarded, while the sediment containing DBSA-BNNTs was collected for further experiments. After centrifugation, the DBSA content could be quantified by the BNNT:DBSA ratio based on the weight loss through TGA analysis. (Figure S5, Supporting Information) The collected DBSA-BNNT sediment, redispersed by bath sonication for 15 min, was concentrated using a vacuum centrifugal concentrator (VISION, VS-802). The water was gradually evaporated until the desired concentration was reached. The phase transition behavior according to BNNT concentration was characterized through polarized optical microscope (Nikon Eclipse LV100N POL).

Fabrication of DBSA-BNNT LC Films: The BNNT film was fabricated with 16 wt.% DBSA-BNNT dispersion (at nematic LC phase). The PET substrate (thickness: 120 µm) was treated with oxygen plasma for 5 min to ensure good wettability of dispersion. The DBSA-BNNT LC was coated onto the PET substrate at a speed of 100 mm s^{-1} using a Dr. blade through a coating knife (KP-3000 VH). The fabricated BNNT films were well adsorbed onto PET after drying overnight, and the final thickness of the films was determined by micrometer measurements and SEM analysis. For comparison, BNNT buckypaper was fabricated via vacuum filtration using a BNNT dispersion (3 mg mL^{-1}) in ethanol without any dispersion stabilizer.

Dispersion Stability Evaluation: The dispersion stability of DBSA-BNNT and SDS-BNNT (Sodium dodecyl sulfate, purchased from Sigma-Aldrich) was characterized by Turbiscan LAB (Formulaction Scientific Instruments, $C_{BNNT} = C_{surfactant} = 0.4$ mg mL^{-1}, scanned every hour).

Estimation of Surfactant Areal Density on BNNT Surface: The areal density of each surfactant on unit area of BNNT surface was calculated based on Thermogravimetric analysis (TGA) measurement and estimated surface area of BNNTs. The TGA was performed using a Q50 (TA Instruments) up to 900 °C in air at a heating rate of 10 °C min^{-1}. The surface area of BNNT used (≈760 m^2 g^{-1}) was calculated from the experimentally measured physical parameters by TEM, which are average diameter of ≈4.5 nm, average length of ≈3 µm, and ≈2.5 walls.

Surface Tension Measurement: The surface tension of surfactants at various concentrations was measured using a contact angle analyzer (Phoenix 300 Touch) through the pendant drop method. To ensure measurement accuracy, each experiment was repeated at least five times using the same drop volume (10 µL). To evaluate the surface tension behavior of BNNT-surfactant dispersion, BNNTs were dispersed with each surfactant (SDS, DBSA) in DI water. Then, the BNNT sediments with bound surfactant, after centrifugation to remove unbound surfactants, were redispersed in DI water. Finally, BNNT dispersions with DBSA 0.2 mM and SDS 1.0 mM concentrations were prepared based on the quantified surfactant content adsorbed on the BNNT surface, as determined by thermogravimetric analysis (TGA). Subsequently, each surfactant was added incrementally at regular intervals, and the changes in surface tension were measured to determine the critical micelle concentration (CMC) of the surfactants in the dispersion.

Characterizations of DBSA-BNNT Film: Surface morphology of BNNTs in high-density DBSA-BNNT film were characterized using a scanning electron microscope (Nova NanoSEM450, FEI company). For visualization of BNNT alignment in the film the orientation J plugin (ImageJ, JAVA) in HSD mode with color mapping, based on SEM images of the BNNT surface was used. The density of the films was calculated by measuring the weight of 5 × 5 cm^2 films.

$$\rho = m/(A \times t) \quad (4)$$

where m is the mass of DBSA-BNNT film, A is the surface area of the film, and t is the thickness of the film by SEM analysis.

The thermal neutron shielding effectiveness values (*Q*) of BNNT films were measured at the thermal neutron facility of the Korea Research Institute of Standards and Science (KRISS). The measurement was conducted by an SP9 ^{3}He proportional counter (Centronic, Ltd) with thermal neutrons generated by collisions between neutrons emitted from a ^{241}Am-Be source and graphite. The energy distribution of these thermal neutrons was calculated using the Monte Carlo N-Particle eXtended code.[91] The shielding effectiveness (*Q*) was calculated by measuring thermal neutron count rates before and after passing through the specimen (R_{1h}, S_{1h}). During this process, a Cd cover was used to separate epithermal neutrons. Finally, the linear attenuation coefficient (μ) was derived.

$$\mu = -(1/t)\ln(1-Q) \tag{5}$$

where t is the thickness of film, and Q is the thermal neutron shielding effectiveness.

The mass attenuation coefficient was calculated by dividing the linear attenuation coefficient by the density of the BNNT films. Specific heat capacity and thermal diffusivity measurements were performed to determine the thermal conductivity of the BNNT films. The specific heat capacity of the BNNT films was calculated by measuring the heat flow of both the sample and a reference material (sapphire) using Differential Scanning Calorimetry (Q20, TA Instruments).

$$C_{ps} = \frac{H}{h} \times \frac{m_r}{m_s} \times C_{pr} \tag{6}$$

where H is the difference between the heat flow of a sample and an empty pan, h is the difference between the heat flow of a sample and reference, m_r is the weight of the reference, m_s is the weight of the sample, and C_{pr} is heat capacity of the sample. Thermal diffusivity was measured using LaserPIT (Advance-RIKO). The thermal conductivity was subsequently calculated using the measured specific heat capacity and thermal diffusivity (K).

$$K = \alpha \times C_p \times \rho \tag{7}$$

where α is the thermal diffusivity, $C_p$is the specific heat capacity, and ρ is the density.

The dose equivalent rate and flux of space radiations through shielding materials were estimated using the On-Line Tool for the Assessment of Radiation In Space (OLTARIS, version 5.01) simulation tool developed by NASA Langley Research Center (LaRC). The radiation environment on Lunar surface was set as GCR model of Badhwar-O'Neill 2020 and histroical 1977 solar minimum.

Supporting Information

Supporting Information is available from the Wiley Online Library or from the author.

Acknowledgements

This work was supported by grants from the Korea Institute of Science and Technology Open Research Program (KIST ORP, 2E33503), Future Security Challenge Technology Development Program through the Korea Institute of Police Technology (KIPoT) funded by the Korean Government (Ministry of Science and ICT, National Police Agency) (RS-2023-00238902), ITECH R&D program of MOTIE/KEIT (project No. 2410000736), Development of the flexible radiation shielding sheets based on high quality BNNT production, and BNNT Composites for Space and Military Applications Research Laboratory of Korea Research Institute for Defense Technology Planning and Advancement, Republic of Korea (KRIT-CT-21-014), and the National Research Foundation of Korea (NRF) grant funded by the Ministry of Science and ICT(MSIT) (No.RS-2025-02315930, Development of Core Technology for Rad-hard Materials, Devices and Characterization). Special thanks to Dr. Seungki Hong for TEM characterization.

Conflict of Interest

The authors declare no conflict of interest.

Data Availability Statement

Data supporting the findings of this study are available from the corresponding author upon reasonable request.

Keywords

boron nitride nanotubes, liquid crystals, neutron shielding, space radiation, surfactant

Received: April 28, 2025
Revised: June 18, 2025
Published online:

[1] N. Iliopoulos, M. Esteban, *Acta Astronaut.* **2020**, *167*, 85.
[2] R. Santomartino, N. J. H. Averesch, M. Bhuiyan, C. S. Cockell, J. Colangelo, Y. Gumulya, B. Lehner, I. Lopez-Ayala, S. McMahon, A. Mohanty, S. R. S. Maria, C. Urbaniak, R. Volger, J. S. Yang, L. Zea, *Nat. Commun.* **2023**, *14*, 1391.
[3] J. Chancellor, C. Nowadly, J. Williams, S. Aunon-Chancellor, M. Chesal, J. Looper, W. Newhauser, *J. Environ. Sci. Health C Toxicol. Carcinog.* **2021**, *39*, 113.
[4] J. L. Hoff, L. W. Townsend, E. N. Zapp, *J. Radiat. Res.* **2002**, *43*, S125.
[5] M. Maalouf, M. Durante, N. Foray, *J. Radiat. Res.* **2011**, *52*, 126.
[6] L. W. Townsend, *Radiat. Prot. Dosimetry* **2005**, *115*, 44.
[7] E. B. Hoglund, J. Carlsson, B. Stenerlow, *E, Int. J. Radiat. Biol.* **2000**, *76*, 539.
[8] A. Takahashi, H. Ikeda, Y. Yoshida, *Int. J. Particle Therapy* **2018**, *5*, 151.
[9] A. R. Kennedy, *Life Sci. Space Res.* **2014**, *1*, 10.
[10] B. Wang, H. Yasuda, *Life* **2020**, *10*, 298.
[11] J. C. Chancellor, R. S. Blue, K. A. Cengel, S. M. Auñón-Chancellor, K. H. Rubins, H. G. Katzgraber, A. R. Kennedy, *npj Microgravity* **2018**, *4*, 8.
[12] A. Gohel, R. Makwana, B. Soni, *IOP Conf. Ser.: Mater. Sci. Eng.* **2022**, *1221*, 012003.
[13] S. A. Thibeault, C. C. Fay, S. E. Lowther, K. D. Earle, G. Sauti, J. H. Kang, C. Park, A. M. McMullen, *Systematic Computational and Experimental Study*, NASA, Hampton VA **2012**.
[14] E. E. Khozemy, E. F. Salem, A. E.-H. Ali, *Radiat. Phys. Chem.* **2022**, *193*, 109976.
[15] K. Rojdev, W. Atwell, R. Wilkins, B. Gersey, F. F. Badavi, *National Space and Missile Materials Symposium*, NASA, Hampton VA **2009**.
[16] S. T. Abdulrahman, Z. Ahmad, S. Thomas, A. A. Rahman, *in Micro and Nanostructured Composite Materials for Neutron Shielding Applications*, Elsevier, Amsterdam / New York **2020**.
[17] C. Zeitlin, *Handbook of Bioastronautics*, Springer, Cham, **2021**.
[18] S. A. Thibeault, J. H. Kang, G. Sauti, C. Park, C. C. Fay, G. C. King, *MRS Bull.* **2015**, *40*, 836.
[19] S. A. Thibeault, C. C. Fay, S. E. Lowther, K. D. Earle, G. Sauti, J. H. Kang, C. Park, A. M. McMullen, *Systematic Computational and Experimental Study*, NASA, Hampton VA **2012**.
[20] J. W. Wilson, F. F. Badavi, F. A. Cucinotta, J. L. Shinn, G. D. Badhwar, R. Silberberg, C. Tsao, L. W. Townsend, R. K. Tripathi, *HZETRN: Description of a Free-Space Ion and Nucleon Transport and Shielding Computer Program*, NASA, Hampton VA **1995**.
[21] F. A. Cucinotta, S. Hu, N. A. Schwadron, K. Kozarev, L. W. Townsend, M. H. Y. Kim, *Space Weather* **2010**, *8*, https://doi.org/10.1029/2010SW000572.

[22] L. Townsend, R. Fry, *Adv. Space Res.* **2002**, *30*, 957.
[23] H. E. Spence, M. J. Golightly, C. J. Joyce, M. D. Looper, N. A. Schwadron, S. S. Smith, L. W. Townsend, J. Wilson, C. Zeitlin, *Space Weather* **2013**, *11*, 643.
[24] D. M. Hassler, C. Zeitlin, R. F. Wimmer-Schweingruber, B. Ehresmann, S. Rafkin, J. L. Eigenbrode, D. E. Brinza, G. Weigle, S. Böttcher, E. Böhm, *Science* **2014**, *343*, 1244797.
[25] L. C. Simonsen, T. C. Slaba, P. Guida, A. Rusek, *PLoS Biol.* **2020**, *18*, 3000669.
[26] C. Zeitlin, D. Hassler, F. Cucinotta, B. Ehresmann, R. Wimmer-Schweingruber, D. Brinza, S. Kang, G. Weigle, S. Böttcher, E. Böhm, *Science* **2013**, *340*, 1080.
[27] D. Golberg, Y. Bando, C. Tang, C. Zhi, *Adv. Mater.* **2007**, *19*, 2413.
[28] J. Wang, C. H. Lee, Y. K. Yap, *Nanoscale* **2010**, *2*, 2028.
[29] D. Golberg, Y. Bando, Y. Huang, T. Terao, M. Mitome, C. Tang, C. Zhi, *ACS Nano* **2010**, *4*, 2979.
[30] Tiano, A. L., C. Park, J. W. Lee, H. H. Luong, L. J. Gibbons, S.-H. Chu, S. I. Applin, et al., *Proc. SPIE* **2014**, *9060*, 906006.
[31] M. B. Jakubinek, K. S. Kim, M. J. Kim, A. A. Martí, M. Pasquali, *J. Mater. Res.* **2022**, *37*, 4403.
[32] J. H. Kim, T. V. Pham, J. H. Hwang, C. S. Kim, M. J. Kim, *Nano Convergence* **2018**, *5*, 1.
[33] C. H. Lee, S. Bhandari, B. Tiwari, N. Yapici, D. Zhang, Y. K. Yap, *Molecules* **2016**, *21*, 922.
[34] S. Kalay, Z. Yilmaz, O. Sen, M. Emanet, E. Kazanc, M. Culha, *Beilstein J. Nanotechnol.* **2015**, *6*, 84.
[35] M. B. Jakubinek, B. Ashrafi, Y. Martinez-Rubi, J. Guan, M. Rahmat, K. S. Kim, S. Dénommée, C. T. Kingston, B. Simard, *Nanotube Superfiber Materials*, Elsevier, Amsterdam **2019**.
[36] C. Park, S.-H. Chu, C. Fay, *NSTRF Student Meeting at JPL*, NASA, Hampton VA **2019**.
[37] E. Cheraghi, S. Chen, J. T. Yeow, *IEEE Nanotechnol. Magazine* **2021**, *15*, 8.
[38] K.-H. Ryu, M. Kang, N.-H. You, S. G. Jang, S. Ahn, D.-Y. Kim, *Adv. Compos. Hybrid Mater.* **2024**, *7*, 159.
[39] P. Snapp, C. Cho, D. Lee, M. F. Haque, S. Nam, C. Park, *Adv. Mater.* **2020**, *32*, 2004607.
[40] J. H. Kang, G. Sauti, C. Park, V. I. Yamakov, K. E. Wise, S. E. Lowther, C. C. Fay, S. A. Thibeault, R. G. Bryant, *ACS Nano* **2015**, *9*, 11942.
[41] M. Foroutan, S. J. Fatemi, S. M. Fatemi, *J. Nanostructure Chem.* **2020**, *10*, 265.
[42] X. J. Zeng, W. L. Liu, *Micro Nano Lett.* **2014**, *9*, 569.
[43] Z. Hanif, K.-I. Choi, J.-H. Jung, A. G. M. Pornea, E. Park, J. Cha, H.-R. Kim, J.-H. Choi, J. Kim, *Ind. Eng. Chem. Res.* **2023**, *62*, 2662.
[44] C. T. Castillo, C. Bruel, J. R. Tavares, *Nanoscale Adv.* **2020**, *2*, 2497.
[45] M. B. Jakubinek, J. F. Niven, M. B. Johnson, B. Ashrafi, K. S. Kim, B. Simard, M. A. White, *Phys. Status Solidi* **2016**, *213*, 2237.
[46] K. S. Kim, M. B. Jakubinek, Y. Martinez-Rubi, B. Ashrafi, J. Guan, K. O'Neill, M. Plunkett, A. Hrdina, S. Lin, S. Dénommée, *RSC Adv.* **2015**, *5*, 41186.
[47] K. S. Kim, C. T. Kingston, A. Hrdina, M. B. Jakubinek, J. Guan, M. Plunkett, B. Simard, *ACS Nano* **2014**, *8*, 6211.
[48] C. Zhi, Y. Bando, C. Tang, D. Golberg, *Solid State Commun.* **2011**, *151*, 183.
[49] N. Behabtu, C. C. Young, D. E. Tsentalovich, O. Kleinerman, X. Wang, A. W. Ma, E. A. Bengio, R. F. Ter Waarbeek, J. J. De Jong, R. E. Hoogerwerf, *Science* **2013**, *339*, 182.
[50] V. A. Davis, A. N. G. Parra-Vasquez, M. J. Green, P. K. Rai, N. Behabtu, V. Prieto, R. D. Booker, J. Schmidt, E. Kesselman, W. Zhou, *Nat. Nanotechnol.* **2009**, *4*, 830.
[51] S. P. Yadav, S. Singh, *Prog. Mater. Sci.* **2016**, *80*, 38.
[52] S. Zhang, S. Kumar, *Small* **2008**, *4*, 1270.
[53] C. J. Simonsen Ginestra, C. Martínez-Jiménez, A. Matatyaho Ya'akobi, O. S. Dewey, A. D. Smith McWilliams, R. J. Headrick, J. A. Acapulco, L. R. Scammell, M. W. Smith, D. V. Kosynkin, *Nat. Commun.* **2022**, *13*, 3136.
[54] H. Lim, Y.-K. Kim, H.-S. Kim, T. Lee, M. M. Hossain, H.-O. Jeong, H. S. Lee, H. Cho, Y. Joo, S. S. Lee, *ACS Appl. Mater. Interfaces* **2023**, *15*, 24681.
[55] A. D. S. McWilliams, C. A. de Los Reyes, L. Liberman, S. Ergülen, Y. Talmon, M. Pasquali, A. A. Martí, *Nanoscale Adv.* **2019**, *1*, 1096.
[56] A. B. Jódar-Reyes, A. Martín-Rodríguez, J. L. Ortega-Vinuesa, *J. Colloid Interface Sci.* **2006**, *298*, 248.
[57] H. Wang, *Curr. Opin. Colloid Interface Sci.* **2009**, *14*, 364.
[58] E. Nativ-Roth, O. Regev, R. Yerushalmi-Rozen, *Chem. Commun.* **2008**, 2037.
[59] C. Richard, F. Balavoine, P. Schultz, T. W. Ebbesen, C. Mioskowski, *Science* **2003**, *300*, 775.
[60] M. J. O'connell, S. M. Bachilo, C. B. Huffman, V. C. Moore, M. S. Strano, E. H. Haroz, K. L. Rialon, P. J. Boul, W. H. Noon, C. Kittrell, *Science* **2002**, *297*, 593.
[61] H. Zhang, S. Yuan, J. Sun, J. Liu, H. Li, N. Du, W. Hou, *J. Colloid Interface Sci.* **2017**, *506*, 227.
[62] M. Gao, N. Du, Z. Yao, Y. Li, N. Chen, W. Hou, *Soft Matter* **2021**, *17*, 2490.
[63] F. Mirri, R. Ashkar, V. Jamali, L. Liberman, R. A. Pinnick, P. Van Der Schoot, Y. Talmon, P. D. Butler, M. Pasquali, *Macromolecules* **2018**, *51*, 6892.
[64] K. S. Kim, M. Couillard, H. Shin, M. Plunkett, D. Ruth, C. T. Kingston, B. Simard, *ACS Nano* **2018**, *12*, 884.
[65] R. A. Chowdhury, S. X. Peng, J. Youngblood, *Cellulose* **2017**, *24*, 1957.
[66] H. A. Badehian, C. Vatankhah, *J. Mol. Struct.* **2022**, *1262*, 133069.
[67] N. J. Hutchinson, T. Coquil, A. Navid, L. Pilon, *Thin Solid Films* **2010**, *518*, 2141.
[68] Y. K. Kim, S. Y. Kim, Y. Joo, S. G. Jang, S. Q. Choi, S. S. Lee, *Small Structures* **2024**, *5*, 2400281.
[69] H. Eskalen, Y. Kavun, S. Kerli, S. Eken, *Opt. Mater.* **2020**, *105*, 109871.
[70] E. Halliwell, C. Couch, R. Begum, W. Li, M. Maqbool, *Colloids Surf. A* **2021**, *622*, 126646.
[71] K. Bellur, V. Konduru, E. F. Medici, D. S. Hussey, D. L. Jacobson, J. M. LaManna, J. S. Allen, C. K. Choi, *J. Flow Visualizat. Image Process.* **2016**, *23*, 1.
[72] T. Yasin, M. N. Khan, *e-Polymers* **2008**, *8*, 059.
[73] R. Adeli, S. P. Shirmardi, S. J. Ahmadi, *Radiat. Phys. Chem.* **2016**, *127*, 140.
[74] D. Lee, J. Kim, B. Park, I. Jo, S.-K. Lee, Y. Kim, S.-B. Lee, S. Cho, *Metals* **2021**, *11*, 413.
[75] R. C. Singleterry Jr, S. R. Blattnig, M. S. Clowdsley, G. D. Qualls, C. A. Sandridge, L. C. Simonsen, T. C. Slaba, S. A. Walker, F. F. Badavi, J. L. Spangler, *Acta Astronaut.* **2011**, *68*, 1086.
[76] S. Zhang, R. F. Wimmer-Schweingruber, J. Yu, C. Wang, Q. Fu, Y. Zou, Y. Sun, C. Wang, D. Hou, S. I. Böttcher, *Sci. Adv.* **2020**, *6*, aaz1334.
[77] N. Grossiord, P. van der Schoot, J. Meuldijk, C. E. Koning, *Langmuir* **2007**, *23*, 3646.
[78] H. Cho, J. H. Kim, J. H. Hwang, C. S. Kim, S. G. Jang, C. Park, H. Lee, M. J. Kim, *Sci. Rep.* **2020**, *10*, 7416.
[79] Z. Király, G. Findenegg, E. Klumpp, H. Schlimper, I. Dékány, *Langmuir* **2001**, *17*, 2420.
[80] E. J. Wanless, W. A. Ducker, *J. Phys. Chem.* **1996**, *100*, 3207.
[81] S. Manne, J. Cleveland, H. Gaub, G. Stucky, P. Hansma, *Langmuir* **1994**, *10*, 4409.
[82] J. N. Israelachvili, D. J. Mitchell, B. W. Ninham, J. C. Society, *Faraday Trans. 2: Mole. Chem. Phys.* **1976**, *72*, 1525.
[83] M. J. Rosen, J. T. Kunjappu, *Surfactants and interfacial phenomena*, John Wiley & Sons, Hoboken,NJ **2012**.
[84] L. Macakova, E. Blomberg, P. M. Claesson, *Langmuir* **2007**, *23*, 12436.
[85] S. M. Bachilo, M. S. Strano, C. Kittrell, R. H. Hauge, R. E. Smalley, R. B. Weisman, *Science* **2002**, *298*, 2361.

[86] J. Scamehorn, R. Schechter, W. Wade, *J. Colloid Interface Sci.* **1982**, *85*, 463.
[87] N. I. Kovtyukhova, Y. Wang, R. Lv, M. Terrones, V. H. Crespi, T. E. Mallouk, *J. Am. Chem. Soc.* **2013**, *135*, 8372.
[88] Y. Wang, Z. Shi, J. Yin, *J. Mater. Chem.* **2011**, *21*, 11371.
[89] D. Lisjak, *Proc. Propert. Adv. Ceramics Compos. VII: Ceramic Trans.* **2015**, *252*, 335.
[90] S.-H. Lee, M. J. Kim, S. Ahn, B. Koh, *Int. J. Mol. Sci.* **2020**, *21*, 1529.
[91] Y. H. Kim, H. Park, Y. K. Kim, J. Kim, J. Kang, *Radiat. Meas.* **2017**, *107*, 73.

Supporting Information

High-Density Boron Nitride Nanotube Composites via Surfactant-Stabilized Lyotropic Liquid Crystals for Enhanced Space Radiation Shielding

Young-Kyeong Kim[1,2,†], Ik Jae Lim[1,2], Hongjin Lim[1], Yongbi Joo[1,3], Jueun Park[1,4], Md Monir Hossain[1], Hyunjin Cho[5], Nam-Ho You[6], Seokhoon Ahn[1], Hunsu Lee[7], Sang Seok Lee[1], Yongho Joo[1], Se Youn Moon[8], Hee Il Yoo[8], Calista Lum[9], Cheol Park[10], Siyoung Q. Choi[2,], and Se Gyu Jang[1,*]*

[1]Functional Composite Materials Research Center, Institute of Advanced Composites Materials, Korea Institute of Science and Technology, Wanju, Jeonbuk 55324, Republic of Korea

[2]Department of Chemical and Biomolecular Engineering, Korea Advanced Institute of Science and Technology (KAIST), Daejeon, 34141, Republic of Korea; KAIST Institute for the NanoCentury, Korea Advanced Institute of Science and Technology (KAIST), Daejeon 34141, Republic of Korea

[3]Department of Chemistry, Gachon University, 1342 Seongnam-daero, Sujeong-gu, Seongnam-si, Gyeonggi-do, 13120, Republic of Korea

[4]Department of JBNU-KIST Convergence, Research Institute of Physics and Chemistry, Jeonbuk National University, Jeonju, 54896, Republic of Korea

[5]Department of Materials and Parts of Secondary Battery, Jeonju Kijeon College, Jeonju 54989, Republic of Korea

[6]Carbon Composite Materials Research Center, Institute of Advanced Composite Materials, Korea Institute of Science and Technology (KIST), Wanju 55324, Republic of Korea

[7]Ramp Convergence Research Center, Institute of Advanced Composites Materials, Korea Institute of Science and Technology, Wanju, Jeonbuk 55324, Republic of Korea

[8]High-enthalpy Plasma Research Center, Jeonbuk National University, 546 Bongdong-ro, Bongdong-eup, Wanju-gun, Jeollabuk-do, 55317, Republic of Korea

[9]Department of Physics, University of California, Irvine, CA, 92697, USA

[10]Advanced Materials Processing Branch, NASA Langley Research Center, Hampton, VA, 23681, USA

*Corresponding author: segyu.jang@kist.re.kr (S.G.J.); sqchoi@kaist.ac.kr (S.Q.C.)

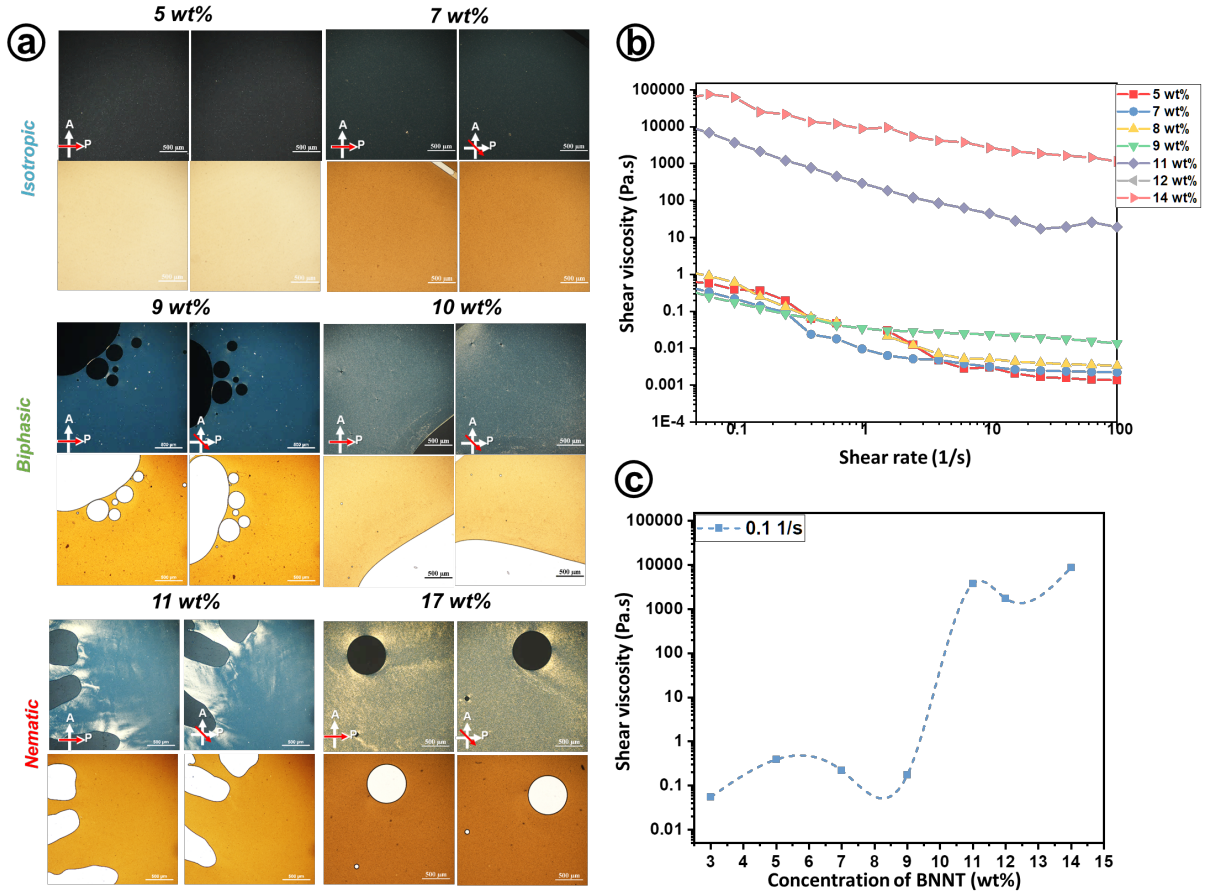

Figure SF1. (a) Polarized optical microscopy (POM) images showing phase transitions from isotropic (5-7 wt%) through biphasic (9-10 wt%) to full nematic (11-17 wt%) phases. (b) Shear viscosity as a function of shear rate of BNNT dispersions at different concentrations, demonstrating the dramatic viscosity increase in full nematic phases at ~ 11 wt%. (c) Shear viscosity at 0.1 s^{-1} plotted against BNNT concentration.

The liquid-crystalline phase behavior of BNNT dispersions was systematically characterized using a combination of polarized optical microscopy (POM) and rheological measurements. In the isotropic region (3–7 wt%), the dispersions did not exhibit birefringence under crossed polarizers, confirming a random orientation of BNNTs. Between 9 and 11 wt%, POM revealed the characteristic coexistence of bright nematic domains within a dark isotropic matrix (biphasic region), as shown in Figure SF1a. At 11 wt%, uniform birefringence was observed throughout the sample, indicating a fully developed nematic phase.

To further confirm the phase transition, we provide rheological data in Figure SF1b, consistent with our previous report. [1]

Rheological measurements were conducted on concentrated BNNT dispersions (3–14 wt%) using a DHR-3 rotational rheometer (TA Instruments) with a cone-and-plate geometry (radius: 40 mm, cone angle: 1°, truncated gap: 54 μm). The Peltier plate was maintained at 25 ° C, and a solvent trap was used to minimize water evaporation. All rheological data were recorded over a 15-second period under steady shear after a stabilization time of several minutes (up to 10 minutes depending on the sample), ensuring a deviation of less than 6% in viscosity values. As shown in Figure SF1c, the shear viscosity at 0.1 s^{-1} remained relatively low in the isotropic region (3–7 wt%) but exhibited a dramatic increase—nearly four orders of magnitude—between 9 and 11 wt%. This sharp rise in viscosity reflects the isotropic-to-biphasic transition at 9 wt% and the biphasic-to-nematic transition at 11 wt%, in agreement with the visual observations from POM analysis. [2] It is noteworthy that the observed transition concentration for DBSA-stabilized BNNTs (~11 wt%) is higher than that for P(VP-r-QVI)-stabilized BNNTs (~7 wt%) reported in our previous study. [1] This difference is likely to be attributed to a lower degree of BNNT debundling by DBSA or a smaller effective excluded volume of DBSA-coated BNNTs compared to that of polymer-coated BNNTs.

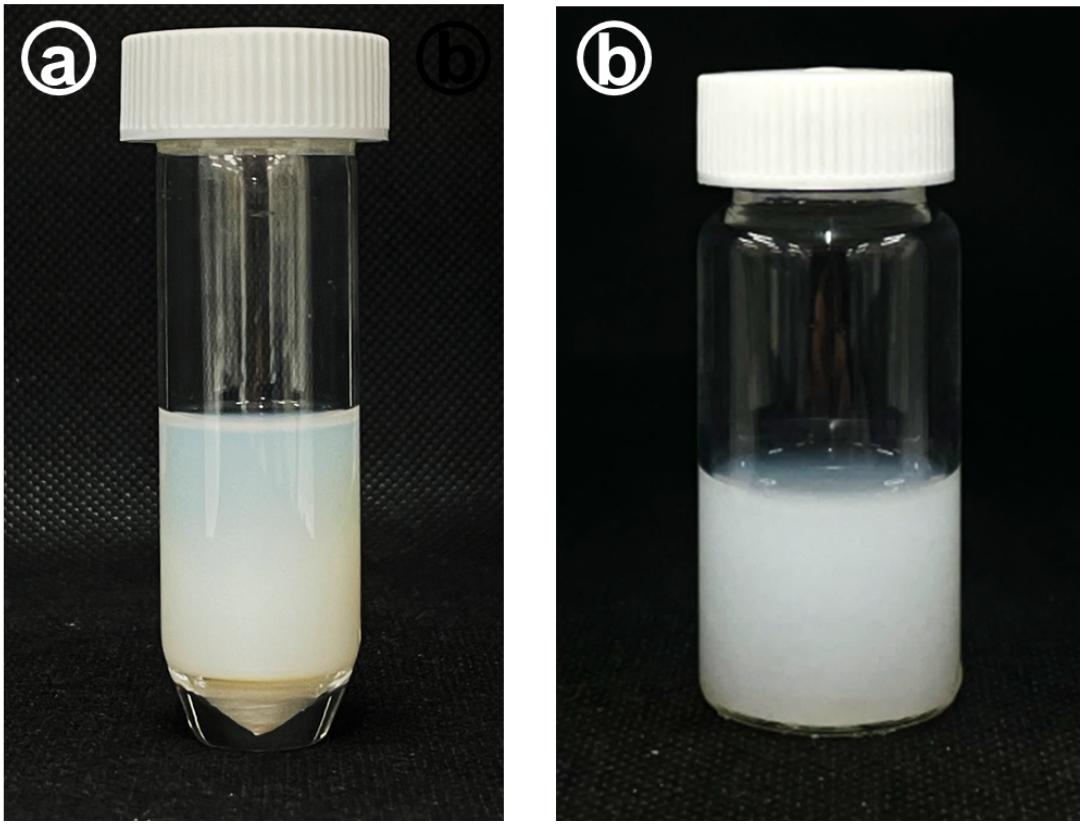

Figure SF2. SDS-assisted BNNT dispersion (a) flocculation at high-concentration BNNT (6 wt%) (b) homogeneous dispersion after redispersion at lower concentration (0.4 wt%).

As observed in Figure SF2a, SDS-assisted BNNT (SDS-BNNT) dispersion exhibited partial aggregation and flocculation at high concentration, resulting in a BNNT concentration gradient observed along the vial height. For redispersion, upon dilution with water, the suspension was diluted to 0.4 wt% and bath-sonicated for 15 minutes. As observed in Figure SF2b, after the redispersion treatment, BNNTs formed a homogeneous dispersion throughout the vial, demonstrating the reversible stability characteristic of depletion-induced flocculation

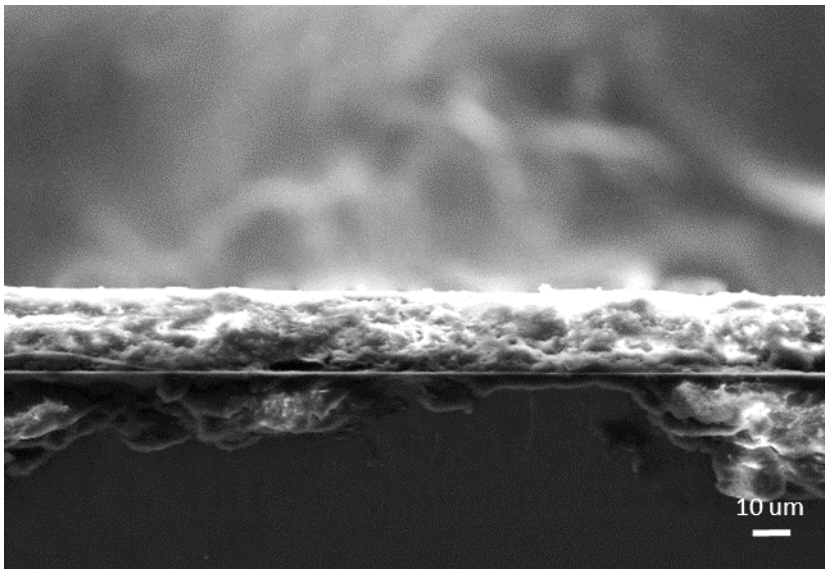

Figure SF3. Cross-sectional SEM image of the BNNT film with a thickness of 20 μm

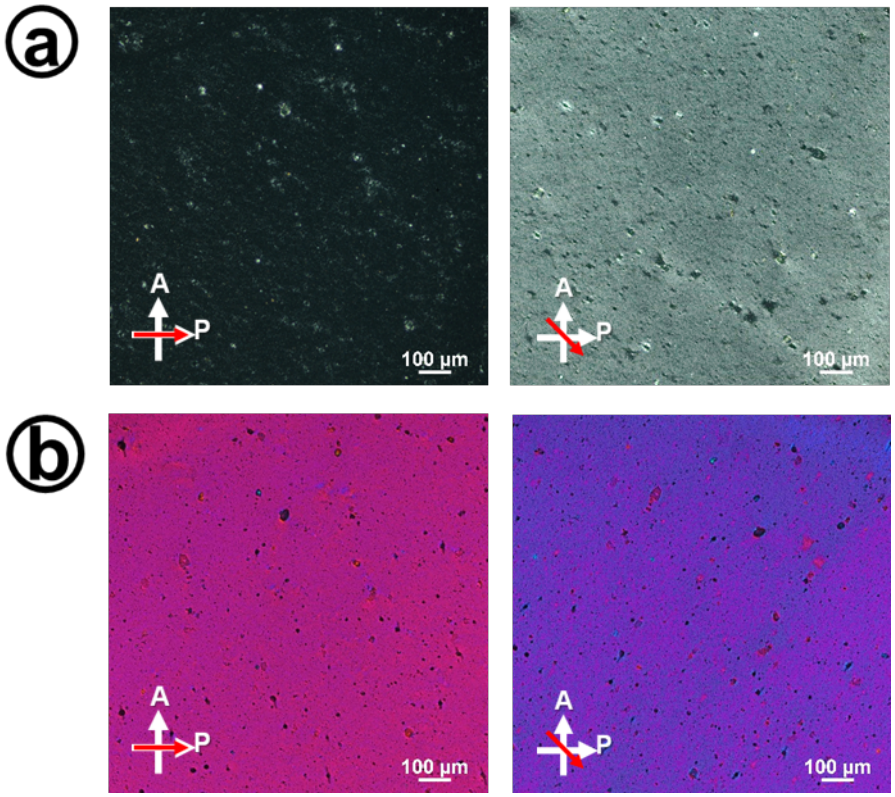

Figure SF4. (a) POM images and (b) POM images with retardation plate of unidirectionally aligned DBSA-BNNT film coated on glass. (~20 um in thickness)

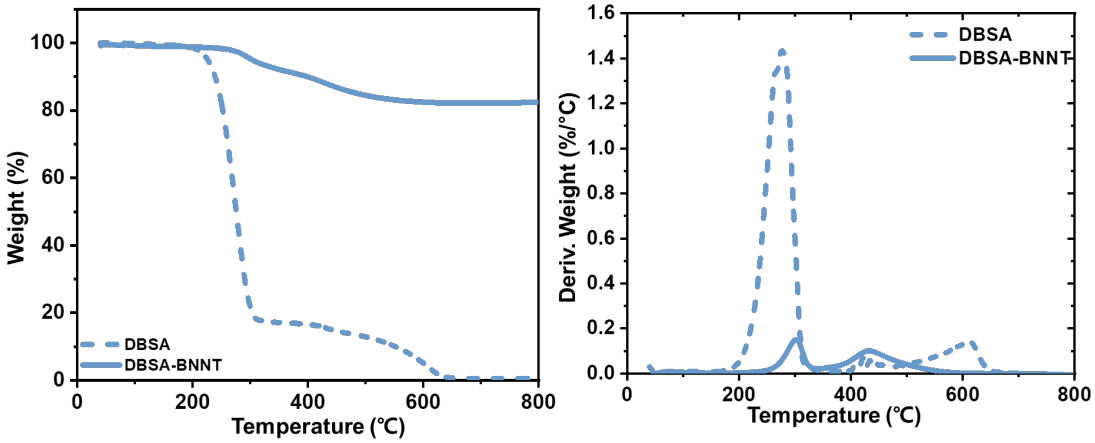

Figure SF5. Thermogravimetric analysis (TGA) of DBSA surfactant and DBSA-BNNT (Left) Weight loss profiles showing thermal decomposition of pure DBSA (dashed line) and DBSA-BNNT (solid line). (Right) Derivative weight loss curves highlighting the decomposition temperature ranges. The DBSA surfactant shows complete decomposition between 200-400°C, while BNNTs remain thermally stable up to 800°C, enabling quantitative determination of surfactant content in DBSA-BNNT suspensions through weight loss analysis.

Supporting Information S1.

The reason we hypothesized the possible formation of a DBSA bilayer on the BNNT surface is that the extraordinarily high colloidal stability of DBSA-stabilized BNNTs, in contrast to SDS-stabilized ones, cannot be explained otherwise. Given the similar molecular structures of the tail groups in SDS and DBSA, such a disparity in colloidal stability at high concentrations suggests that the adsorption behavior of the two surfactants is fundamentally different. Although we are unable to present direct visual evidence of bilayer formation, we summarize below the indirect evidence and rationales that support our interpretation.

1. **High surface areal density of DBSA estimated via TGA and surface area measurement:** We believe the TGA measurement of the amount of DBSA adsorbed on BNNT is relatively accurate, as free DBSA molecules in the dispersion medium were removed by centrifugation and decantation of supernatant. The observed mass loss in the TGA experiment is attributed solely to DBSA decomposition, given the exceptional thermal stability of BNNTs up to 800 °C. As the reviewer correctly pointed out, an accurate estimation of BNNT surface area is critical for calculating the surface areal density of surfactants. However, due to the presence of residual impurities such as cages and hexagonal boron nitride, even after purification, precise analysis of BNNT dimensions and polydispersity is challenging. Therefore, we measured the external surface area of freeze-dried BNNTs using t-plot BET characterization (Micromeritics), yielding a value of approximately 160 m^2/g. This is comparable to the surface area of multi-walled carbon nanotubes (100–150 m^2/g). Based on this surface area, the calculated areal density of DBSA on BNNT is approximately 25 molecules/nm^2, which is unrealistically high considering the van der Waals radius of the sulfonate head group allows a maximum density of about 4 molecules/nm^2 (as noted in the manuscript). We attribute this overestimation to the bundling of BNNTs during freeze-drying, which reduces the measured surface area.

As the BNNTs used in this study are multi-walled, their true surface area is not expected to exceed the known value for single-walled CNTs (~1000 m^2/g). If we use 1000 m^2/g for our calculation, the areal density becomes ~4 molecules/nm^2, the maximum packing density for sulfonate head groups. This density is significantly higher than reported values for single-chain surfactants on CNT surfaces (2.2–2.7 molecules/nm^2), where surfactants typically form hemispherical micelles with hydrophilic heads exposed to the aqueous phase (as discussed in the manuscript). Thus, using a reasonable intermediate surface area (~760 m^2/g) leads to a calculated density that strongly suggests bilayer formation on the BNNT surface.

2. **Stronger adsorption affinity of DBSA over SDS:** As shown in Figures 5b and 5c, DBSA shows a stronger adsorption affinity to BNNTs than SDS. Given the similarity in tail group structures, this difference is unlikely due to hydrophobic/hydrophilic interactions. We suggest that this higher affinity of DBSA arises from specific interactions between the sulfonic acid head group and the BNNT surface, as discussed in the manuscript. If the inner layer of DBSA is adsorbed via its head group, with the tail facing the aqueous phase, then the formation of a bilayer through interdigitation is thermodynamically favorable to maintain dispersion stability.
3. **High-resolution TEM and EDX analysis:** Due to limited access to cryo-TEM, we used high-resolution TEM to characterize DBSA-stabilized BNNTs. The sample was prepared by drop-casting the dispersion onto a holey carbon TEM grid. As expected, direct imaging of the surfactant bilayer was unsuccessful due to the low electron density of the organic molecules. Nonetheless, EDX mapping revealed that the BNNTs (identified via HAADF, boron, and nitrogen EDX mapping images on the top of Figure) were fully covered with organic material (identified via carbon and oxygen EDX mapping images on the bottom of Figure), suggesting the presence of surfactant.

While this does not directly prove bilayer formation, it provides supporting evidence for the adsorption of DBSA onto the BNNT surface.

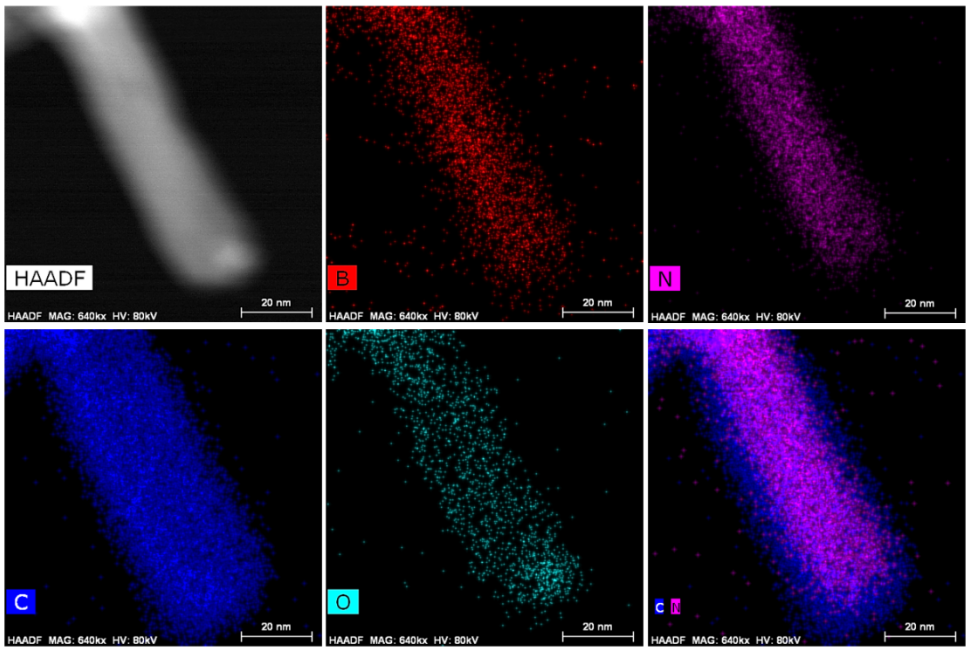

Supporting Information S2.

The initial suspension was prepared by dispersing BNNT (3 mg/ml) and DBSA (3 mg/ml, 9.2 mM) in DI water (23.4 ml). In this process, DBSA molecules adsorb onto the BNNT surface and excess DBSA molecules simultaneously exist in the dispersion medium. To address the concentration of DBSA in the dispersion, we measured pH values of the dispersions at different preparation procedures. The measured pH of the initial dispersion, including DBSA-stabilized BNNTs and free DBSA molecules in the dispersion media was about 2.4. The subsequent centrifugation induces physical phase separation, dividing the system into a supernatant including predominantly free DBSA molecules in the dispersion media and a sediment comprising DBSA-stabilized BNNTs on the bottom of the conical tube. Then, the supernatant (measured pH ~ 2.5) containing excess free DBSA was decanted, and the sediment including DBSA-stabilized BNNTs was redispersed in an equal volume of deionized water (23.4 ml) with no addition of extra surfactants. The measured pH of the redispersed DBSA-stabilized BNNTs dispersion was ~ 3.5.

To provide quantitative evidence for the methodology, we calculated DBSA concentrations before and after centrifugation using pH measurements and established acid-base equilibrium relationships. It is noteworthy that DBSA molecules are aggregated as micelles or vesicles at over critical concentration as well as acid-soap dimer formation of DBSA molecules at high concentration occurs, resulting in difference in estimated and experimentally measured concentrations. Nonetheless, relative amounts of DBSAs in supernatant and residual DBSAs in redisersed BNNTs are roughly estimated.

DBSA is a strong acid surfactant and, therefore, follows the dissociation equilibrium DBSA $\rightleftharpoons H^+ + DBSA^-$, where the total DBSA concentration can be determined using the relationship $C\_total = [HA] + [H^+]$, with $[HA] = [H^+]^2/Ka$. Since literature reports of DBSA pKa values vary from 0.7 to -0.45, we analyzed using both values to ensure the reliability of our

calculations. Using pKa = 0.7 (Ka ~ 0.1995), the calculated DBSA concentrations based on measured pH values were ~ 4.06 mM for the initial dispersion (pH 2.4), ~ 3.21 mM for the supernatant (pH 2.5), and a ~ 0.32 mM for the redispersed DBSA-stabilized BNNTs (pH 3.5). When using pKa = -0.45 (Ka ~ 0.3548), the calculated values were ~ 4.02 mM for the initial dispersion, ~ 3.19 mM for the supernatant, and ~ 0.32 mM for the redispersed DBSA-stabilized BNNTs, showing similar results.

In both cases, the difference in calculated amounts using pH values between DBSAs in initial dispersion before centrifugation (~4.06 mM when Ka is 0.7) and residual DBSAs in redispersed dispersion (4.06 – 3.21 = 0.85 mM, when Ka is 0.7) is approximately 20 %. These residual DBSA molecules are either bound on the surface of BNNTs or freely dispersed in the dispersion media at equilibrium.

Reference

[1] H. Lim, Y.-K. Kim, H.-S. Kim, T. Lee, M. M. Hossain, H.-O. Jeong, H. S. Lee, H. Cho, Y. Joo, S. S. Lee, *ACS Applied Materials & Interfaces* **2023**, 15, 24681.

[2] S. Onogi, T. Asada, in *Rheology: Volume 1: Principles*, Springer, 1980.